ISSN No. 0737-5352-68

OBJECTIVE ESTIMATION OF TROPICAL CYCLONE WIND STRUCTURE FROM INFRARED SATELLITE DATA

Kimberly J. Mueller
Thomas H. Vonder Haar

Funding for this research was primarily sponsored by CIRA Activities and Participation in GOES I-M Produce Assurance Plan under NOAA cooperative agreement NA17RJ1228. Further support was provided by Improvement in Deterministic and Probabilistic Tropical Cyclone Surface Wind Predictions under NOAA cooperative agreement NA17RJ1228.

CIRA Cooperative Institute for Research in the Atmosphere

Colorado State University

OBJECTIVE ESTIMATION OF TROPICAL CYCLONE WIND STRUCTURE FROM INFRARED SATELLITE DATA

Submitted By

Kimberly J Mueller
Colorado State University.
Cooperative Institute for Research in the Atmosphere

In partial fulfillment of the requirements
For the Degree of Master of Science
Colorado State University
Fort Collins, CO
Summer 2004

ABSTRACT

Objective Estimation of Tropical Cyclone Wind Structure From Infrared Satellite Data

Given the destructive nature of tropical cyclones, it is extremely important to provide quality estimates of intensity, as well as wind structure. The Dvorak technique, and an automated version, the Objective Dvorak Technique (ODT) use a method of identifying cloud characteristics from satellite images (visible and infrared), to provide estimates of current storm intensity. However, these IR techniques provide no information on the extent or location of damaging winds. Estimates of wind structure via alternate methods have significant disadvantages. Gathering data using aircraft is expensive; therefore storms are flown only if they are an immediate threat to the U.S. AMSU algorithms for estimating wind structure have proven successful, however the instruments fly aboard polar-orbiting satellites, which only pass over the tropics twice a day, and are not contiguous at or near the equator.

It is apparent that an alternate method of estimating wind structure is necessary; one in which data coverage is continuous. While IR data has historically been used to estimate intensity, the goal of this research is to extend the use of IR data to estimate wind structure. Theoretically, there should be a solid relationship between deep convection and the extent of damaging winds. The database for this work includes aircraft reconnaissance data from 91 Atlantic and E. Pacific storms flown during the 1995-2003 seasons as ground truth, in combination with GOES IR imagery, and storm best track information. Using multiple linear regression techniques, with predictors derived from the IR data, a radius of maximum wind can be estimated, as well as, more accurately, the symmetric tangential winds at a radius of 200 km (size parameter). These estimated parameters are then fit to a modified combined Rankine vortex model to reconstruct the entire symmetric wind field. Given the storm motion vector, and researched relationships between storm motion and wind asymmetries, the asymmetric part of the wind field can be calculated and added to the symmetric part to provide an estimation of the entire tropical cyclone wind field.

Kimberly Joanne Mueller
Department of Atmospheric Science
Colorado State University
Fort Collins, CO 80523
Fall 2004

THESIS OUTLINE

Chapter 1 – Introduction

Over the course of the past century, with the aid of ship reports, satellites, radar, buoys and aircraft reconnaissance, location and intensity forecasting of tropical cyclones (TC's) has improved dramatically, resulting in a substantial reduction in loss of life. In recent years, the annual death toll in the United States has averaged between 50 and 100 persons (Ahrens, 1999), however with increased tourism and population density in coastal states, it is becoming increasingly important to produce accurate intensity, wind structure, and track forecasts in order to protect against loss of both life and property. Furthermore, Goldenberg *et al.* 2001 (G01) note that there has been an increase in Atlantic basin TC occurrence recently due to increases in sea surface temperatures (SST's), associated with a shift in the thermohaline circulation. The broad periodicity of this shift indicates that this upward trend could influence TC frequency for many decades to come. While the 2001-2003 seasons were not particularly overactive, the 1995-2000 seasons combined are the most active on record. The threat of increasing hurricane frequency, coupled with increasing coastal populations, drive the continual study of hurricane intensity and wind structure forecasting.

Aircraft reconnaissance is perhaps the best method of estimating hurricane winds. Air Force Reserve and NOAA aircraft fly into the Atlantic Basin, including the Gulf of Mexico and the Caribbean Sea, and Eastern Pacific Basin storms to provide *in situ* measurements of wind, pressure, temperature, and storm position. The job of the reconnaissance crews is to transmit vital information on storm location, strength, size and motion via satellite to the National Hurricane Center. However, due to a lack of funds,

most TC's are only flown when they become a threat to U.S. land, and are rarely flown outside of the Atlantic and Eastern Pacific Basins. Obviously there is a need for an equally reliable observation platform that is available at all times at all locations.

As a result, forecasters often turn to a method developed by Vernon Dvorak in the mid 1970's. The goal of Dvorak was to provide estimates of both the current and future intensity of tropical cyclones, by identifying cloud characteristics from satellite imagery. He employed a model of tropical cyclone development that consists of a set of curves representing intensity change with time, and certain cloud features associated with the cyclone at different lifetimes (see Figure 1.01). These curves were derived empirically by relating satellite intensity estimates to those obtained from official storm histories and reconnaissance data (Dvorak, 1974). Hurricane development and weakening are proposed to occur along one of three paths (rapid, typical, slow) which are plots of T-numbers with time, and development and weakening are assumed to be occurring in a homogeneous environment. If, for instance, there appears to be significant sea surface temperature changes, or a change in shear, the expectation must be modified.

The specific cloud features used in the analysis are categorized into central features (CF) and outer banding features (BF). These two parameters taken together, with an estimate of cloud depth, comprise what Dvorak terms a T number, which describes the current intensity of the cyclone. After a current intensity analysis is made, cloud features associated with the cyclone's vertical motions and inflow/outflow are used to make an intensity *forecast*. Typically, an intensifying hurricane will have a very bright comma shape to it, indicating deep convection in the central core. Furthermore, the cirrus bands will appear to be spreading out from the central features (see Figure 1.02).

Dvorak also studied current synoptic scale situations to aid him in his forecasts. Obviously, however, since this method relies on image pattern recognition, it involves some subjectivity on the part of the forecaster.

In the years since Dvorak developed his original technique, scientists have been attempting to automate the method in an effort to produce results that are more objective. Following an initial impetus by Dvorak himself to use digital IR data to better the above method, Christopher Velden and Timothy Oleander of CIMSS, along with Ray Zehr of NOAA/NESDIS at CIRA, developed a method called the Objective Dvorak Technique (ODT). A computer based algorithm within the McIDAS system utilizes several functions to read and analyze GOES IR satellite data to compute and output an intensity estimate for a targeted tropical cyclone (Velden et al, 1998).

The Geostationary Operational Environmental Satellites (GOES) have instruments aboard capable of measuring infrared radiation emitted from the Earth. Satellite instruments typically measure infrared radiation between wavelengths of about 3 μm and 20 μm. This radiation measurement can then be used to make an estimate of the brightness temperature of any clouds within the view of the satellite. The ODT uses these brightness temperature measurements, along with a computer algorithm, to assign an intensity estimate to a tropical cyclone, in a method analogous to Dvorak's study of cloud patterns. This technique is not valid for tropical depressions or weak tropical storms. Forecasters around the globe use this, or similar methods everyday to identify and objectively analyze tropical cyclone intensity. While this automated method can be argued to be an improvement because it does not rely on the subjective human eye recognizing certain features, but rather relies on an objective computer pattern

recognition scheme to assign intensity information, the ODT method is only of comparable accuracy to the simple Dvorak technique (Zehr, 2004). This result leads to the broad conclusion that since Dvorak developed his methods in the 1970's, there has been very little progress made on the use of digital infrared satellite data in the study of tropical cyclones.

While ODT and other similar methods provide vital information about TC intensity, a harder parameter to estimate from IR satellite data alone is the actual TC wind *structure.* At operational forecast centers, TC wind structure is primarily determined by such parameters as the radius of maximum winds, and the radii of 34, 50 and 64 knot winds. These values provide information on how far damaging winds extend from the eyewall of the TC. Other parameters can also be used to quantify TC wind structure. For the purposes of this research, the wind speed at the outer most radii resolvable using the aircraft data (about 200 km) is used as a proxy for the size of the storm. Strong winds at a distance of 200 km from the storm center are indicative of a large storm, while weak winds signify a smaller storm. It is reasonable to assume that infrared satellite data will provide information on TC structure via connections between the extent and strength of deep convection, and the extent of damaging winds.

While there is a deficit of research revolving around the use of infrared data, beginning with the 1997 hurricane season, the Cooperative Institute for Meteorological Satellite Studies at the University of Wisconsin-Madison began demonstrating the derivation of real-time GOES low-level cloud drift winds in the vicinity of Atlantic tropical cyclones. The winds are derived from tracking low-level clouds in sequential, high-resolution GOES visible channel imagery (Dunion and Velden, 2001). These cloud

drift winds provide essential coverage in the outer radii of the hurricane, where conventional observations like buoys and ships are sparse. Since then, GOES cloud drift winds have been assimilated into the Hurricane Research Division (HRD) surface wind analysis. As noted above, cloud drift winds are important for periphery estimations, however they provide little to no information about winds near the eye of the hurricane, because the cirrus shield tends to block tracers at close radii.

Furthermore, it has been demonstrated that satellite measurements in the microwave portion of the electromagnetic spectrum have been integral in TC wind structure algorithm development. Since NOAA launched the Advanced Microwave Sounding Unit (AMSU) aboard their polar-orbiting satellite series in May 1998, passive microwave warm core measurements of tropical cyclones have been successfully made. The science behind the measurement is that vertical temperature soundings can yield valuable information about the mean sea level pressure and wind fields within a tropical cyclone through thermodynamic and dynamic constraints (Brueske and Velden, 2003).

Demuth et al. (2004), derived a method for objectively estimating TC wind radii via a statistical procedure utilizing AMSU-derived parameters. While AMSU is capable of providing this valuable data, since it is a polar-orbiting satellite, it only passes over the tropics twice a day, and is not contiguous at or near the equator. Therefore, while AMSU instruments fly aboard several NOAA satellites, the instruments can still miss a tropical cyclone on one of its passes, and the cyclone will not be observed. Obviously, a rapidly deepening cyclone will exhibit dramatic changes between passes and a missed pass can be very detrimental to forecasters. Another disadvantage of the microwave instrument is that the horizontal resolution is at best 48 km at nadir, and closer to 100 km near the

limbs. Upper tropospheric warm anomalies can be on scales that are smaller than this, and thus not entirely resolvable by the instrument.

From the above discussion, it is clear that while aircraft reconnaissance, visible and microwave data can provide valid information about TC wind structure, observations may not be continuously available, and may not be available near the storm center. A major advantage of using infrared satellite data to observe tropical cyclones is that the coverage is nearly continuous over the global tropics, whereas polar orbiters only pass over a storm twice a day on average, and is available where ship and aircraft data are not. While IR data has been used traditionally to estimate storm intensity (the widely used Dvorak Technique and ODT), the aim of this investigation is to extend the use of IR data to estimate storm structure.

The outline of this research is as follows. Given a digital IR image, a storm position (including latitude, longitude, and estimation of the maximum wind) and the direction and translational speed of the TC, it is hypothesized that an accurate estimateof the wind field (symmetric and asymmetric parts) can be made. From this input, the radius of maximum wind and the symmetric tangential wind speed at a radius of 202km (size parameter) will be estimated. These estimated parameters are fit to a Rankine vortex model to reconstruct the entire symmetric wind field. Given the storm motion vector, and known relationships between storm motion and wind asymmetries, the asymmetric part of the wind field can be estimated, and added to the symmetric part to recreate the entire TC wind field. The database used to develop this algorithm includes 89 cases of Atlantic and east Pacific tropical cyclones from 1995-2003, that have aircraft reconnaissance data available as ground truth.

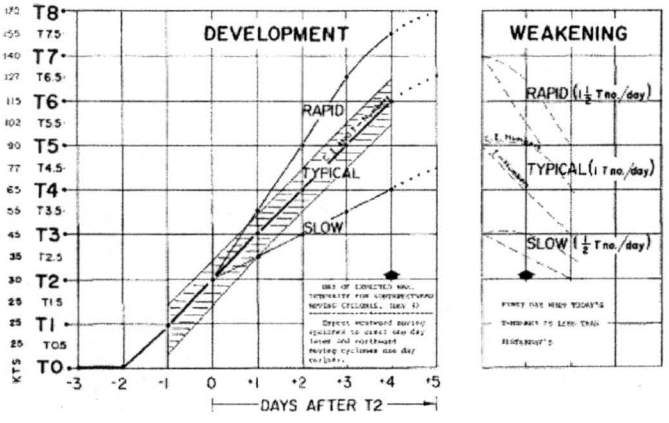

Figure 1.01 Dvorak Intensity Curves
(Dvorak, 1975)

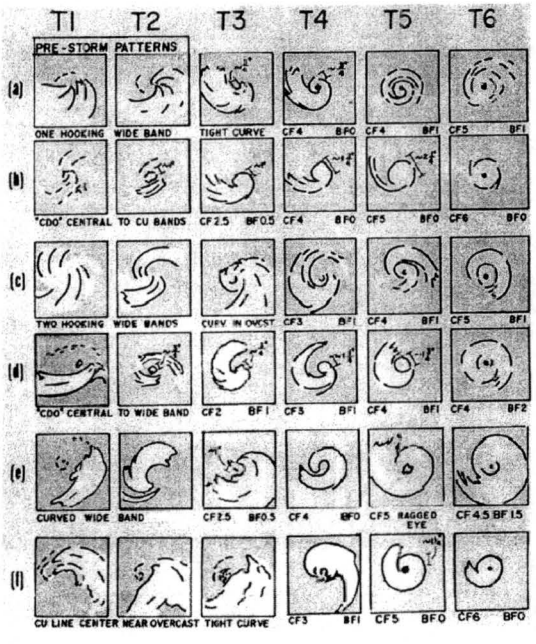

Figure 1.02
Common tropical cyclone cloud patterns and their corresponding T numbers.
(Dvorak, 1975)

CHAPTER 2 – DATA

2.1 Aircraft Reconnaissance Data

Because data are needed from areas where it is impractical, and often impossible, to operate ground based observation stations, the Air Force aerial weather reconnaissance aircraft often fly long routes to collect and transmit weather observations. Currently, the National Oceanic and Atmospheric Administration (NOAA), as well as more frequently Air Force Reserve personnel at Keesler AFB, Miss., have the responsibility in the Department of Defense for aerial weather reconnaissance, including hurricane reconnaissance.

The Air Force uses a fleet of WC-130 aircraft to accomplish these missions, which are equipped with the *Improved Weather Reconnaissance System (IWRS)*. Special weather sensors mounted on these aircraft measure temperature, dewpoint, barometric pressure, actual (radar-measured) altitude of the aircraft, and winds, and calculate a complete weather observation every 10 seconds. Furthermore, the IWRS computers are connected to the aircraft navigation system in order to obtain an exact position for each observation. A key part of the IWRS system is the ability to send data to the National Hurricane Center (NHC) in Miami for analysis and initialization of forecast models. There is an option of viewing and saving data at up to one-second intervals if needed, however data is regularly archived at 10-second intervals.

Because this study aims to diagnose hurricane wind structure, the use of the aircraft reconnaissance wind observations as ground truth was a very important component of the research. The winds are computed aboard the aircraft from a variety of

sensors. There are two probes measuring changes in pressure across the openings in each probe to compute true airspeed and side-slip, while the navigator's *Self-Contained Navigation System* provides ground speed and heading information to complete the wind calculation (www.keesler.com).

This data all gives the user a picture of the storm at flight level. In a developing storm, missions are flown at low levels (500-1500 feet), however as a storm gains strength, the aircraft are forced to fly at higher altitudes (5000 feet is customary) in order to avoid dangerous downdrafts that could force the aircraft too close to the ocean surface.

The Air Force flies a special pattern known as an Alpha Pattern (see figure 2.1). Starting in the northwest quadrant, the aircraft actually fly a diagonal route across the storm to the southeast quadrant, 105 nautical miles on either side of the eye. Next, it is a simple case of always making left turns, so the aircraft doesn't have to fight the winds that are swirling counter-clockwise. The first turn to the left takes the aircraft to the northeast quadrant, at which point the final left turn takes it diagonally across the eye to the southwest quadrant. Notice that after two passes through the eye (fixes), the winds in all four quadrants have been measured. At this point, the plane would typically continue the alpha pattern, making two more fixes before heading home.

2.2 Passive Infrared Remote Sensing

All of the information received by a satellite sensor about the earth and its atmosphere is received in the form of electromagnetic energy (Kidder and Vonder Haar, 1995). The electromagnetic spectrum is defined as a continuum of all types of

electromagnetic radiation in which each type of radiation is ordered according to its *wavelength* (see Figure 2.03).

Divisions in the spectrum have grown out of the various methods for sensing each type of radiation:

Visible (VIS) portion:	0.4 μm to 0.7 μm (400 to 700 nanometers)
Infrared (IR) portion:	0.7 μm to 14 μm
Microwave (MW) portion:	1 mm to 1 m

Remote sensing systems operate in one of several of the visible, infrared, or microwave portions of the electromagnetic spectrum. In the visible portion, features are observed by virtue of reflected solar energy. By contrast, in the infrared portion, sensing of emitted energy predominates. Infrared waves include thermal radiation, that is radiation emitted from the earth and the atmosphere, including clouds. One important characteristic of the infrared channels, over the visible channels, is their ability to provide images at night. This provides continuous coverage of cloud evolution over a full 24-hour period (Kidder and VonderHaar, 1995).

Remote sensing data acquisition of surface features is limited to the 'non-blocked' spectral regions of the electromagnetic spectrum referred to as atmospheric windows (see Figure 2.02). Atmospheric windows define wavelength ranges in which the atmosphere is particularly transmissive of energy. The visible region of the electromagnetic spectrum resides within an atmospheric window in the wavelength range of about 0.3 to 0.9 μm while emitted energy from the earth's surface is sensed through windows at 3 to 5 μm and 8 to 14 μm. Radar and passive microwave systems operate through a window region of 1 mm to 1 m.

Because clouds absorb and emit as near perfect blackbodies in the infrared portion of the electromagnetic spectrum, when clouds are present the infrared radiation being emitted from the cloud is coming from ONLY the cloud top. Emission from lower levels of the cloud is immediately absorbed by adjacent layers of the cloud. Therefore, the radiation that reaches the satellite instrument is related to the temperature at cloud top ONLY. This is why T_b is often referred to as *cloud top temperature (CTT)*. High cloud tops are often indicative of convection and associated severe weather. The higher the cloud top, the colder the temperature at which the cloud is emitting. Thus, intense hurricanes, in which there is significant convection in the eye wall and spiral bands, will exhibit colder CTT's. This is an important proxy measure for tropical cyclone severity, and will be used in this study as a proxy for the storm structure as well.

The most common infrared channels for meteorological satellites are in the 10-12.5 micron window, in which the atmosphere is relatively transparent to radiation upwelling from the Earth's surface. (See Figure 2.02) When the word 'infrared' is used alone to describe an image, it is nearly always in the 10-12.5 micron window, rather than in another portion of the electromagnetic spectrum (Kidder and VonderHaar, 1995).

Normally in satellite image processing, images are displayed such that the greater the radiance, the brighter the pixel. However, because the atmosphere cools with height, and cold objects radiate much less than warm objects do, high cold cloud tops would appear very dark relative to the warm land surface, using the above convention. Therefore, infrared images are typically inverted, meaning that less radiant pixels appear brighter than more radiant pixels. This way, high clouds appear very bright, which is more appealing for the human eye, and easier to interpret. Furthermore, infrared images

are often color enhanced to aid interpretation. Figures 2.03 and 2.04 are color-enhanced images from the CIRA IR archive, illustrating two tropical cyclones. Notice that high, cold cloud tops appear bright red, which corresponds to a radiating temperature of approximately –70 C^0, while the surrounding ocean appears gray, corresponding to radiating temperatures on the order of 20 to 30 C^0.

2.3 CIRA Infrared Archive

An assessment of geostationary IR Imagery of tropical cyclones is described by Zehr (2000). There are normally five geostationary satellites positioned along the equator, giving nearly global coverage (see figure 2.04). Geostationary satellites have the necessary time resolution and the unique capability of pinpointing the exact locations of intense updrafts by monitoring overshooting cold cloud tops.

The CIRA IR Archive includes GOES-7,8,9,10, Meteosat-5,7, and GMS, and uses the satellite that provides the best coverage for a particular TC. The GOES suite of satellites provide coverage over the western portion of the Atlantic Ocean, and a large extent of the Pacific Ocean. Meteosat, run by EUMESAT, provides coverage over the Eastern Atlantic Ocean, and western portions of the Indian Ocean. GMS, a Japanese satellite, provides coverage over the waters surrounding Japan and Australia (see Figure 2.04). All digital images are 4 km resolution Mercator remaps in MCIDAS format with 1-byte pixels. Image size is 640 elements by 480 lines. The standard time interval between images is 30 minutes (Zehr, 2000). The location of the sector is changed as necessary to keep the center of the TC no more than four degrees latitude within the edge of the image. The time period of coverage begins with the first assignment as a Tropical

Depression and ends with the last advisory time. There are seldom gaps of more then 3 hours. Figures 2.04 and 2.05 are examples of images in the CIRA archive.

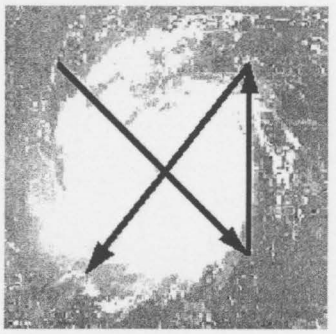

Figure 2.01 Alpha Pattern

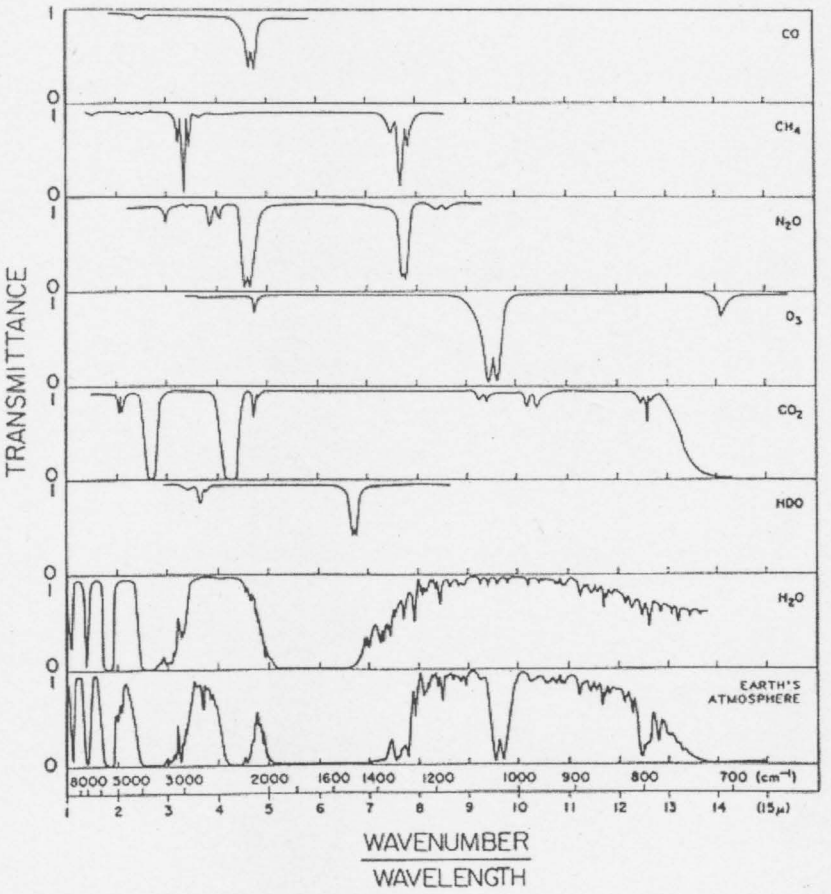

Figure 2.02 Atmospheric Transmittance in the IR; from Kidder and VonderHaar,1995

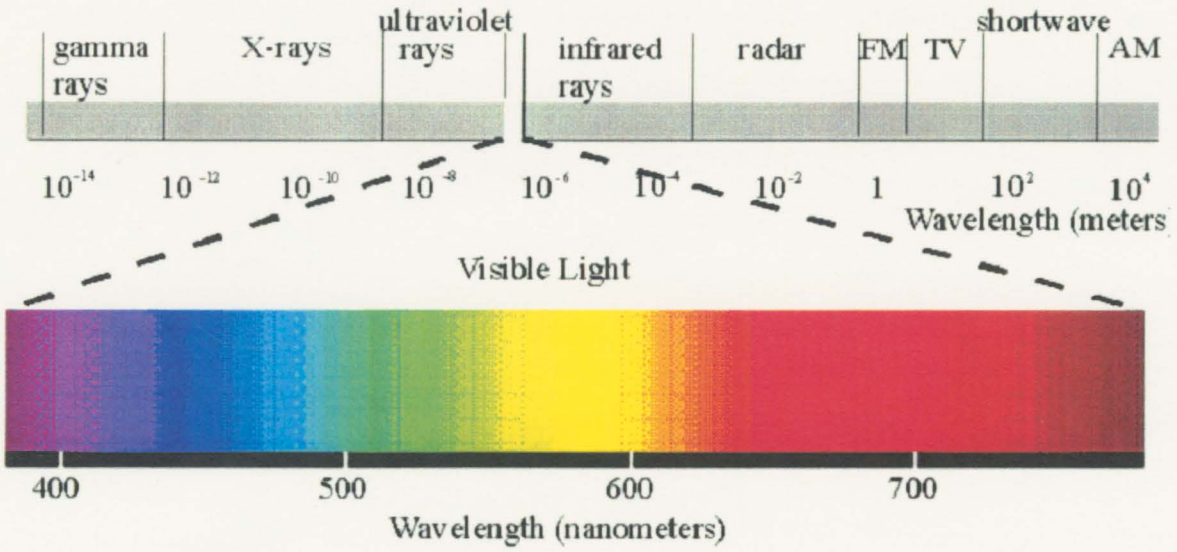

Figure 2.03
Electromagnetic Spectrum

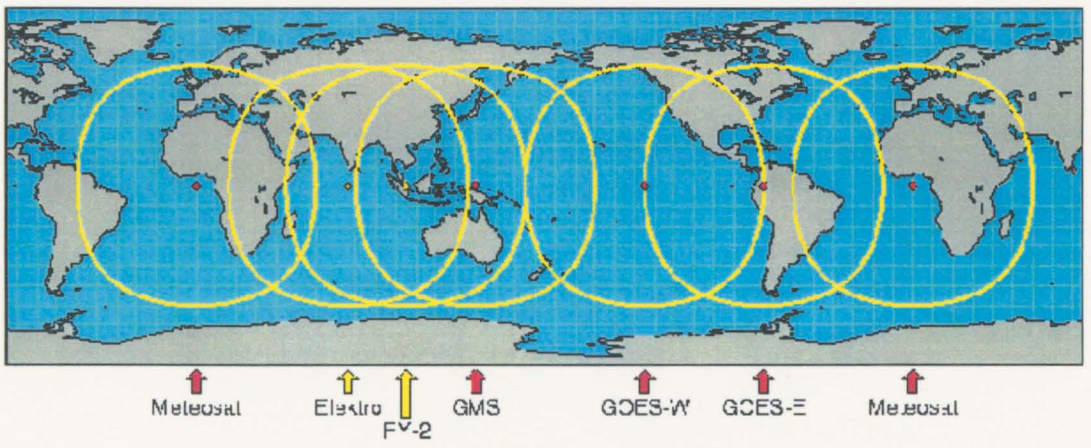

Figure 2.04
Geostationary Satellite Coverage

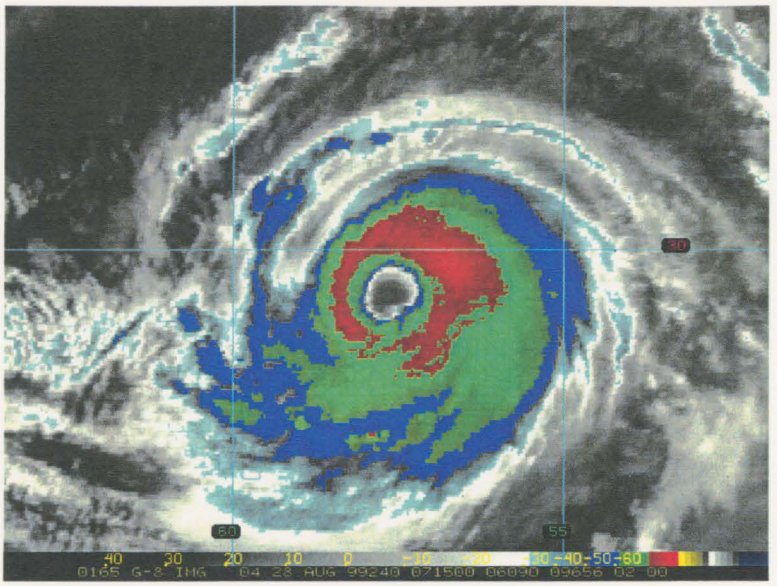

ESTIMATED MINIMUM CENTRAL PRESSURE 948 MB
EYE DIAMETER 35 NM
MAX SUSTAINED WINDS 115 KT WITH GUSTS TO 140 KT

64 KT	75NE	75SE	50SW	50NW
50 KT	175NE	175SE	100SW	125NW
34 KT	275NE	275SE	175SW	200NW

12 FT SEAS 400NE 400SE 200SW 225NW
ALL QUADRANT RADII IN NAUTICAL MILES
(Courtesy of NHC)

Figure 2.05
Hurricane CINDY – 0715 UTC 28 Aug 99

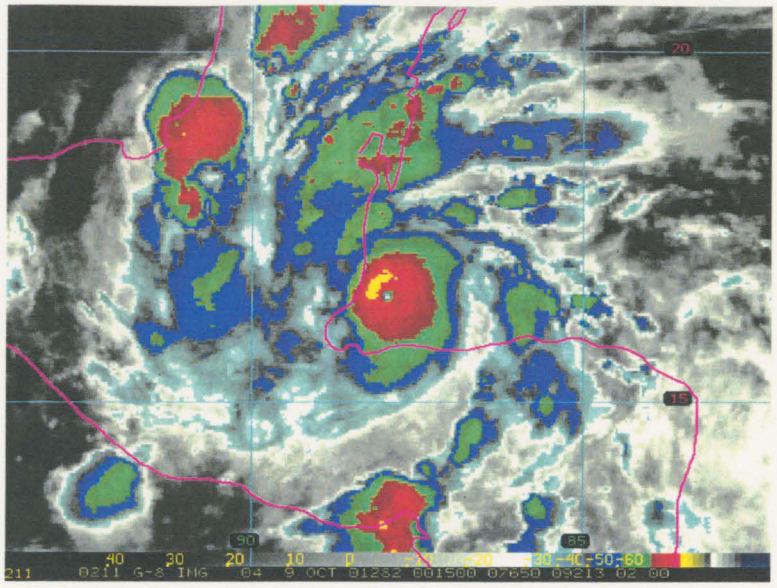

ESTIMATED MINIMUM CENTRAL PRESSURE 954 MB
MAX SUSTAINED WINDS 120 KT WITH GUSTS TO 145 KT.

64 KT	15NE	15SE	10SW	15NW.
50 KT	25NE	25SE	15SW	25NW.
34 KT	125NE	50SE	40SW	60NW.

12 FT SEAS 200NE 150SE 0SW 0NW.
WINDS AND SEAS VARY GREATLY IN EACH QUADRANT. RADII IN NAUTICAL MILES ARE THE LARGEST RADII EXPECTED ANYWHERE IN THAT QUADRANT.
(Courtesy of NHC)

Figure 2.06
Hurricane IRIS – 0015 UTC 9 Oct 01

CHAPTER 3 – DATA PROCESSING

3.1 Initial Treatment of the Data

The aircraft data used in this research comes directly from the NHC air force reconnaissance archive. The data used encompasses a large sampling of Atlantic Basin TC's during the 1995-2003 seasons, as well as a smaller sampling of Eastern Pacific TC's over the same time period. There are 89 total storms in the dataset. The air force may fly the same storm several times, depending on how much of a threat it is to land, and how long lived it is, therefore there may be several flight logs for one storm. Each flight log is therefore concatenated into one file per storm, however there may be data gaps during periods where the storm was not being observed.

For each storm, the aircraft data is composited over twelve hour intervals. This time interval is chosen so that enough observations are be available to perform an objective analysis. It is optimal too because if a larger time interval is chosen, it is possible that the character of the storm has changed to such a degree that combining of the data over the time interval is not truly representative of the storm.

3.2 Storm – Relative Coordinate System

Because a twelve hour time interval is chosen, several air force reconnaissance flights may have been flown during the interval, and several separate center fixes may have been made due to the motion of the storm over the time period. An example of an air force reconnaissance raw wind field of TC Lili in 2002 is shown in figure 3.01. One can see that in earth relative coordinates, there are three distinct centers of circulation, indicating that three separate flights were flown during this twelve hour time period. It is therefore necessary to adjust all data to storm relative coordinates.

To identify the storm center, the NHC best track data is used. The best track data is derived post storm using all available data on the TC, and gives a best estimate for storm position and intensity at six hour increments over the lifetime of the TC. The center location at the time of each wind observation is determined by linear interpolation, and the distance east and north of the center is calculated for that observation. If no best track data is available for the given ending time, no analysis is performed. This storm relative data is assumed to be representative of the wind structure at the end of the 12-hour interval. An example of storm-relative winds is shown for the same Lili case in '02 in Figure 3.02.

3.3 Error Checking

Several error checks were built into the aircraft analysis, in order to maintain a quality dataset. First, several gross error checks were employed to remove data points where the information is clearly unrealistic. These error checks are performed on the modified raw data that is obtained directly from the air force, prior to any analysis. First, any data points in which the wind direction was missing were removed from the dataset. Furthermore, data points where the measured wind speed was less then zero were removed. Wind direction was measured using degrees, from 0 to 360. Any cases in which the recorded wind direction was greater than 360 degrees were removed. Another important gross error check was concerning the altitude of the plane at the time of the measurement. Typically, aircraft fly at 700 hPa in mature tropical storms, and sometimes lower in tropical depressions. However, they do "ferry" to the storm, during which time they typically fly above 500 hPa. Therefore, since we are not interested in measurements taken during this ferrying period, all data points at which the altitude was greater than

5000 m where removed from the dataset. Finally, gross errors in speed were checked. Category five hurricanes, which are extremely rare, can attain wind speeds of greater than 135 knots. Therefore, it is necessary to remove data points at which wind speeds are too great to be realistic. The threshold chosen was 175 knots, which is quite conservative. Once these gross error checks are performed, the x and y coordinate system is converted to a radial and azimuthal coordinate system, and winds are decomposed to radial and tangential components.

Next, it is necessary to determine if there is sufficient data within a specified time period to perform an accurate analysis. A routine was created to determine the maximum azimuthal range without any data. Typically, an aircraft will fly the alpha pattern, therefore, there will be four tangential legs to interpolate data from. However, aircraft are not continuously flying storms, and during a given 12 hour time period, perhaps only one leg is flown. One tangential leg is not sufficient to perform an entire storm analysis. First, this routine finds the maximum azimuthal data gap as a function of radius. It returns a value for how many legs in the azimuth are data free for each radius. Next, the routine calculates how many adjacent radii contain gaps of MORE than 180°. If the dataset is missing 180° of data in the azimuth for four or more adjacent radii, then the entire dataset is thrown out. It is deemed that there is insufficient data to proceed with an analysis

If the dataset passes both the gross error check and the azimuthal gap error check, then a preliminary objective analysis is performed on both the radial and tangential wind speed components. A routine was created to perform a variational analysis of the wind speed observations to obtain values for wind speed on an evenly spaced grid. The

analysis grid consists of 50 data points in the radial direction at 4 km spacing, and 16 data points in the azimuthal direction with a spacing of 22.5 degrees. The objective analysis routine minimizes the difference between the winds on the analysis grid interpolated to the observation points and the original observations. Smoothness constraints provide values on the data void portions of the analysis grid. Further details of the objective analysis can be found in DeMaria et al (1999).

Once the preliminary analysis is performed, another error check is built into the program to identify bad data not identified by the gross error checks. A routine checks for additional bad data by assigning zero weight to observation grid points where the difference between the observed value and that from preliminary analysis is greater than 50 knots. Basically, if the analyzed grid point value is drastically different than the observed value, it indicates that the observed value at that grid point was drastically different than the surrounding grid point observed values. The difference can be manifested as either an inaccurate measurement of the speed or direction of the wind. If the percentage of bad points in the dataset is greater than 10 % , the entire dataset is thrown out, and the analysis is halted, and no analysis output file is created for that storm during that time period. Out of 680 twelve hour time periods during which aircraft were flying the storms in the dataset, only 436 of these cases passed the error checking process.

Once all of the error checks are passed, a final objective analysis is performed on the aircraft data. It is the same routine that is described above as the preliminary analysis, however this time the bad observation data points are set to zero weight, so they have no effect on the interpolation. These analyses are written out to a new file per twelve hour

period in the lifetime of the storm, to later be compared the IR data. An example of an analyzed wind field for the Lili '02 case is shown in Figure 3.03. Figure 3.04 is an isotach plot of the analyzed wind field.

3.2 Matching of the IR data

The analysis of the aircraft data produced a total of 436 accurate wind analysis files for storms from 1995-2003. At this point, these aircraft files must be matched to CIRA IR archive files that cover the same 12-hour portion of the storm's lifetime. Once a match is found, the IR data is read into the analysis. If there is more than one IR image that matches the aircraft analysis time period, than the IR images are averaged. Of the 436 possible analysis files, 249 cases were matched with IR images, and became a member of the final dataset.

The final members of the dataset were further analyzed in terms of both the wind profiles of each storm during each twelve hour analysis period, as well as information on the IR properties. The maximum wind (smax), radius of maximum wind (rmax), azimuthally averaged maximum wind (samax), azimuthally averaged radius of maximum wind (ramax), and radii of 34 knot (r34), 50 knot (r50) and 64 knot (r64) for each storm quadrant were calculated from the aircraft wind analysis file. The IR data was analyzed to provide information on the percent of pixels colder than a certain threshold for each radii. As with the aircraft data, the IR data were calculated at each radii starting at two km, and ending at 202 km, with four km spacing. The brightness temperature thresholds are zero C^o, -10 C^o, -20 C^o, etc, to –70 C^o. Basically, this means that if a large percentage of the pixels in a particular radius is cold, then the cloud tops are quite high, and there is

probably intense convection occurring somewhere along that radial band. The larger the percentage, the greater the extent of the convective activity in the radial band.

For example, Hurricane Cindy in Figure 2.06 and Hurricane Iris in Figure 2.05 both exhibit minimum pressure values near 950 mb, and maximum sustained winds of 115-120 knots. However, the area coverage of cold clouds in Hurricane Cindy is much larger than that for Iris. This means that convection is occurring on a much broader scale in Hurricane Cindy, but producing the same intensity as a storm with more confined areas of convection. Most importantly, the 34 kt wind radii for Cindy are on the order of 200-275 nm for each quadrant, in contrast to the 60-100 nm 34 kt wind radii in the much smaller, but equally intense Iris. This is an illustration of an apparent relationship between cold cloud shield and wind radii. In the next two sections, it will be determined whether quantitative relationships between the IR parameters and the wind structure parameters from the aircraft data can be found.

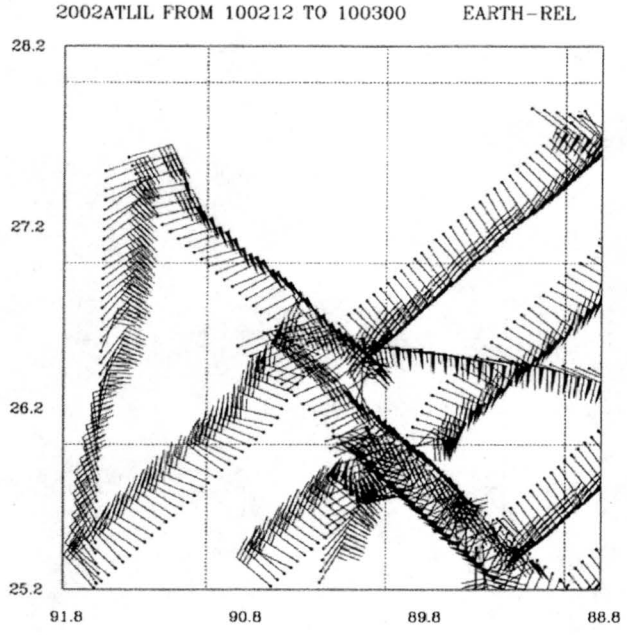

Figure 3.01
TC LILI Earth Relative Wind Field as measured by air force reconnaissance over the twelve hour time period from October 2nd at 12Z to October 3rd at 00Z.

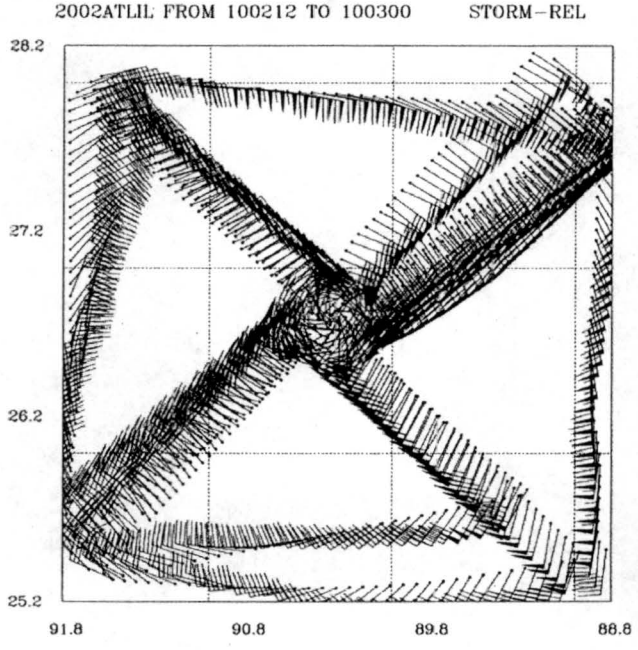

Figure 3.02
TC LILI Storm Relative Wind Field derived using besttrack center fixing for the twelve hour time period from October 2nd at 12Z to October 3rd at 00Z.

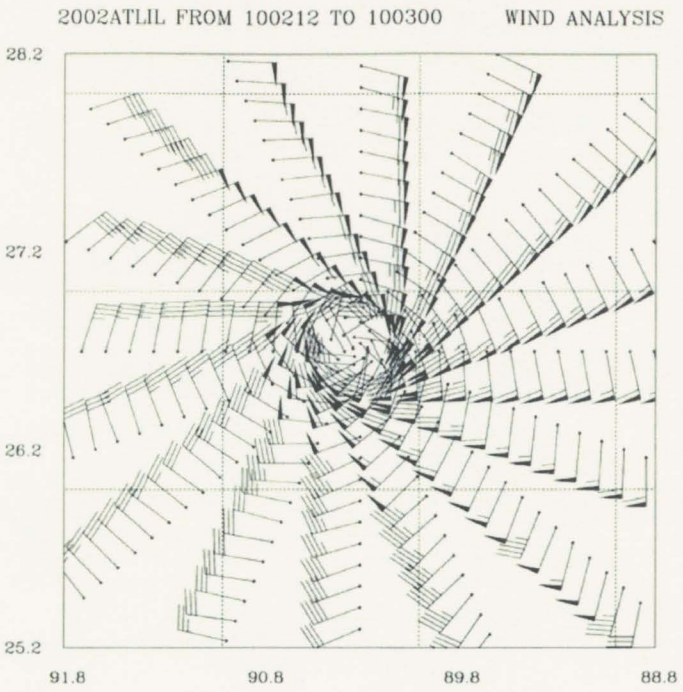

Figure 3.03
TC LILI Wind Analysis for the twelve hour time period from October 2nd at 12Z to October 3rd at 00Z.

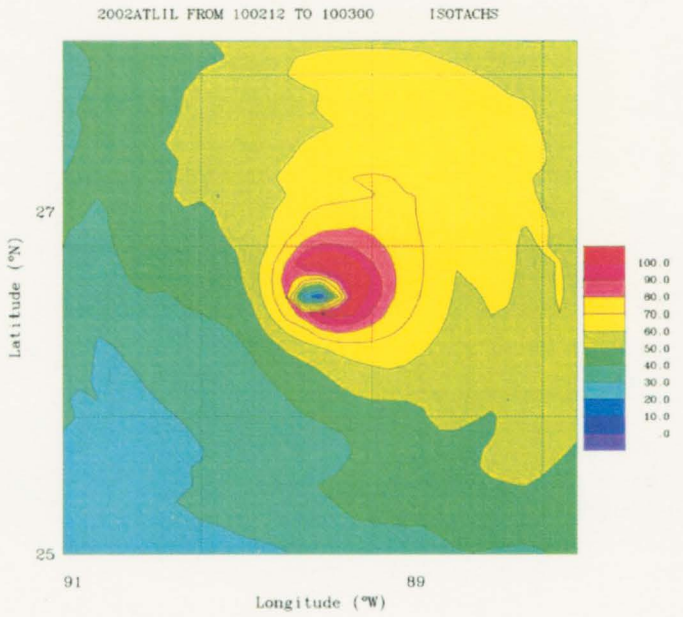

Figure 3.04
TC LILI Isotachs for the twelve hour time period from October 2nd at 12Z to October 3rd at 00Z.

CHAPTER 4 – SYMMETRIC WIND FIELD ANALYSIS

The first step in the analysis is to use the infrared brightness temperature (BT) data to produce an estimate of the radius of maximum wind, and the symmetric wind speed at 202 km. These two parameters, along with an estimate of the maximum wind speed calculated using the Dvorak method from the IR image, can then be fitted to a Rankine vortex model to recreate the entire symmetric wind field.

4.1 DATA

A set of possible predictors is derived using the infrared brightness temperature data, as well as storm latitude, and an estimate of the maximum wind. For the development phase, a maximum wind estimate is derived from aircraft data, however in real-time, a maximum wind can be estimated directly from the IR data via the Dvorak method. As mentioned in chapter 3, the infrared brightness temperature data is reported as a percentage of pixels colder than a particular threshold at each radius from 2 km to 202 km, at 4 km intervals. The threshold values are 0, -10, -20, -30, -40, -50, -60 and –70 C^{o}. An azimuthally averaged brightness temperature is also reported for each radius above.

From this information, several relevant parameters can be derived. First, a storm total percentage of pixels colder than each of the above thresholds is calculated. This yields an overall estimation of the amount of convective activity in the tropical cyclone.

Next, a radius of coldest temperature, as well as a coldest temperature value, are calculated for each storm case.

The following list of parameters makes up the list of possible predictors derived from the infrared data for estimating a radius of maximum wind (RMAX) and a wind speed at a radius of 202 km (V202):

MXWND:	Azimuthally Averaged Maximum Wind Speed
CLD0:	Percent Pixels Colder than 0 C^o
CLD10:	Percent Pixels Colder than -10 C^o
CLD20:	Percent Pixels Colder than -20 C^o
CLD30:	Percent Pixels Colder than -30 C^o
CLD40:	Percent Pixels Colder than -40 C^o
CLD50:	Percent Pixels Colder than -50 C^o
CLD60:	Percent Pixels Colder than -60 C^o
CLD70:	Percent Pixels Colder than -70 C^o
CLDTB:	Azimuthally Averaged Temperature of Coldest Radius
RDCLD:	Azimuthally Averaged Radius of Coldest Temperature
LAT:	Storm Center Latitude

The above parameters represent subsets of the information available in the IR data. An alternate method for finding common patterns in datasets is derived through the use of matrix methods from linear algebra. Empirical Orthogonal Function (EOF) analysis seeks structures that explain the maximum amount of variance in two dimensional datasets. For the purposes of this research, one dimension in the data set represents characteristic spatial structures that vary with time, which is what we seek, and

the sampling dimension is time. The EOF analysis produces a set of structures in the first dimension, which are called the EOF's, and which can be thought of as being the structures in the spatial dimension. The amplitude of the set of structures in the sampling dimension (time) are called the principal components (PC's), and they are related one-to-one to the EOF's.

Singular Value Decomposition (SVD) is used on the data to simultaneously compute both the EOF's and PC's. SVD produces a set of singular values for the data, as well as arrays containing EOF and PC values in the following manner.

Any real rectangular matrix can be represented as the product of the following three matrices:

$$A = U\Sigma V^T$$

Where A = M x N data matrix

$U = M \times N$

$\Sigma = M \times N$

$V = N \times N$

The decomposition of A can be done using eigenanalysis such that:

$$U,V = AA^T, A^TA$$

If M is the sample space (ie time), the EOF's correspond to the columns in the V matrix, which are simply the eigenvectors of the covariance matrix, A^TA, of the original data. Similarly, the PC's are the columns in U, or the eigenvectors of the covariance matrix, AA^T. The vector Σ represents the singular values of the data, which are actually the square roots of the eigenvalues. The singular values are useful in assessing the percent of variance explained by each EOF of the data.

EOF analysis of the normalized infrared data yields the following additional set of possible predictors:

PC1TB:	Leading PC of Azimuthally Averaged Brightness Temperature
PC2TB:	Second Leading PC of Brightness Temperature
PC3TB:	Third Leading PC of Brightness Temperature
PC1GTB:	Leading PC of the Gradient of Brightness Temperature
PC2GTB:	Second Leading PC of the Gradient of Brightness Temperature
PC3GTB:	Third Leading PC of the Gradient of Brightness Temperature

As a first test of the EOF techniques, it was applied to the symmetric tangential winds from the objective analysis. Figure 4.01 represents the first three leading EOF's of the tangential wind data for all storms analyzed. Again, EOF analysis picks out structures that explain a significant amount of variance in the original data. EOF 1, the black curve on the plot, represents the background mean wind field in a TC. EOF 2 is hypothesized to represent the strong winds in the eyewall of the hurricane. Note that the sign of the EOF is arbitrary. The negative maximum in EOF 2 near a radius of 12 km represents a tangential wind maximum at the approximate radius that the eyewall would be located at in an average size, average strength TC. EOF 3 is hypothesized to represent strong winds in the spiral bands of the hurricane, as illustrated by negative maximum near a radius of 50 km.

Figure 4.02 illustrates the amount of variance explained by the first ten EOF's, and it is clear that the majority of the variance is explained by the first three EOF's. In fact, greater than 80% of the variance is explained by EOF1 alone, and another 12.6% is explained by EOF2. The first two EOF's capture a large majority of the variance in the tangential wind field, and this variance is likely related to the location of the radius of maximum winds. In this study, the EOF analysis of the aircraft analyzed tangential wind field is important primarily in determining if the wind structure can be explained by a relatively small number of patterns. Figure 4.02 confirms this is true.

Of greater importance is the EOF analysis of the BT data, as this data will be used as possible predictors for diagnosing the wind field. See Figure 4.03. Like EOF1 of the tangential wind, EOF1 of the BT appears to be a manifestation of the mean cold cloud shield. EOF2 is more interesting. Again, knowing that the sign of the EOF is arbitrary, it appears as though EOF2 is the negative of reality. The peak near the storm center represents a very cold cloud shield, which gradually warms at greater radii. This EOF is important, because a bigger cold cloud shield represents a bigger storm. Therefore, EOF2 may yield important information on the size of the TC, which is an important parameter needed to reproduce the wind field. Finally, EOF3 appears to represent a cold TB maximum near a radius of 75 km, possibly representing the cold cloud tops associated with convection in large eye walls or the spiral bands of the TC. Figure 4.04 illustrates the variance explained by the first ten EOF's. It is clear that the first three EOF's explain nearly 96% of the structural variance in the BT data, therefore they will be retained for further analysis.

It is important to note the similarities between the EOFs of the tangential wind and BT. If the sign of the signal is ignored, and only the amplitude is noted, one can see that EOF1 in both cases picks up the background signal, EOF2 seems to pick up features associated with eyewall convection, and EOF3 illustrates features apparently associated with spiral banding convection. It is concievable, therefore, that the EOFs of BT can be used to effectively predict structures in the tangential wind field.

Finally, the radial gradient of the BT (GTB) field was calculated for each storm in the dataset, and the EOF's of the GTB were calculated, and are illustrated in figure 4.05. In theory, the gradients in the brightness temperature field can provide important information on the wind structure in the storm. Areas in which the gradient is large are characterized by a sharp change in BT over a short distance, indicating a transition from an area of deep convection, to a calmer region of the storm, or vice versa. Typically winds are stronger in areas coincident with deep convective bands, especially in the eyewall, and drop off with a decrease in convection. Therefore, structures in the GTB field may be related to structures in the tangential wind field.

Finally, SVD was done on the gradients of brightness temperature. Gradients were calculated by simply measuring the rate of change of the azimuthally averaged brightness temperature between the two radii adjacent to the point in question. See Figure 4.05. EOF1 of GTB appears to illustrate the rapid decrease in cloud top temperature as one moves away from the eye to the eyewall, which is usually coincident with an area of maximum convective activity, and very cold cloud tops. EOF2 of GTB appears to capture the eyewall convection, and the increase in temperature outside this area of very strong convection.

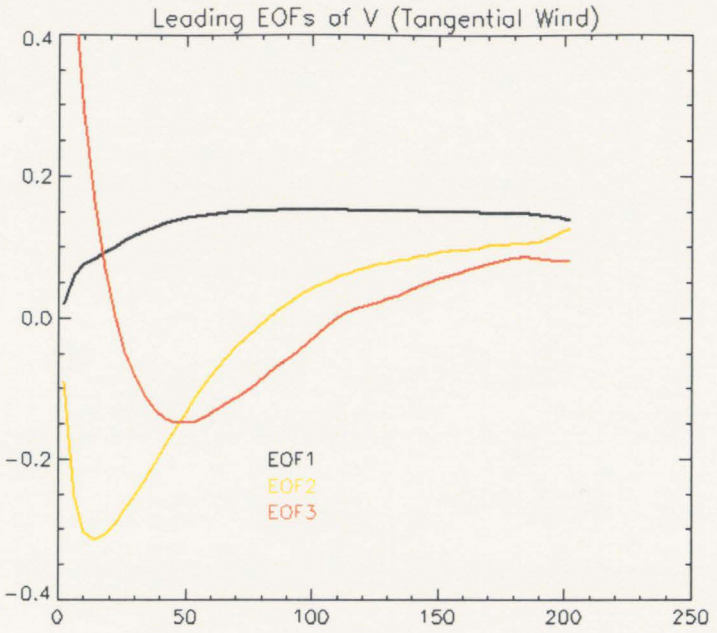

Figure 4.01

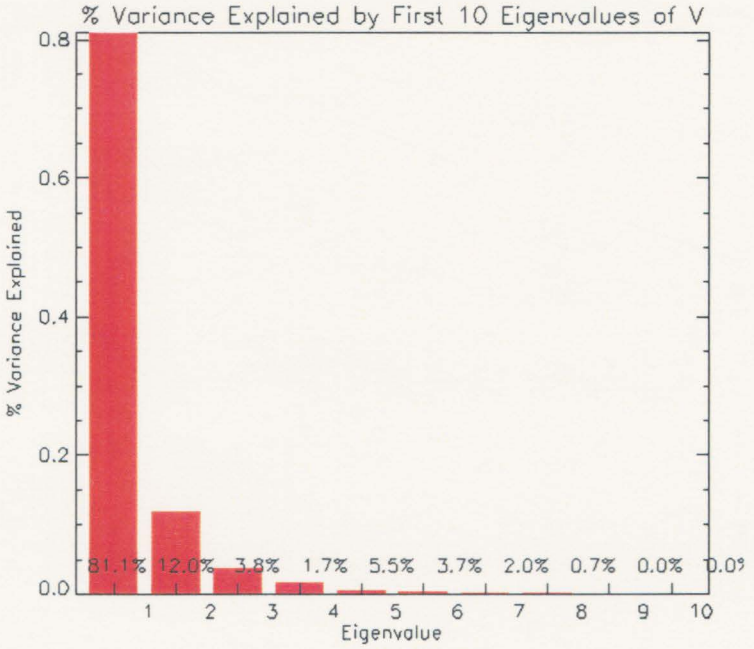

Figure 4.02

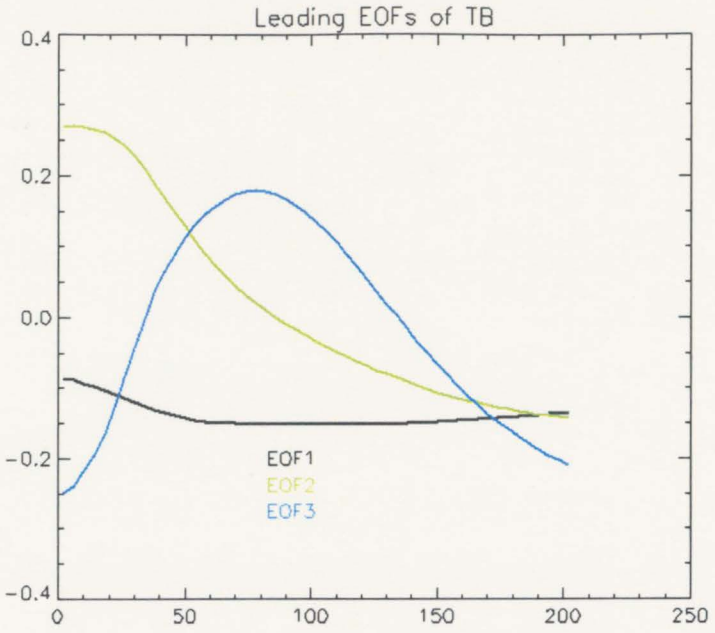

Figure 4.03

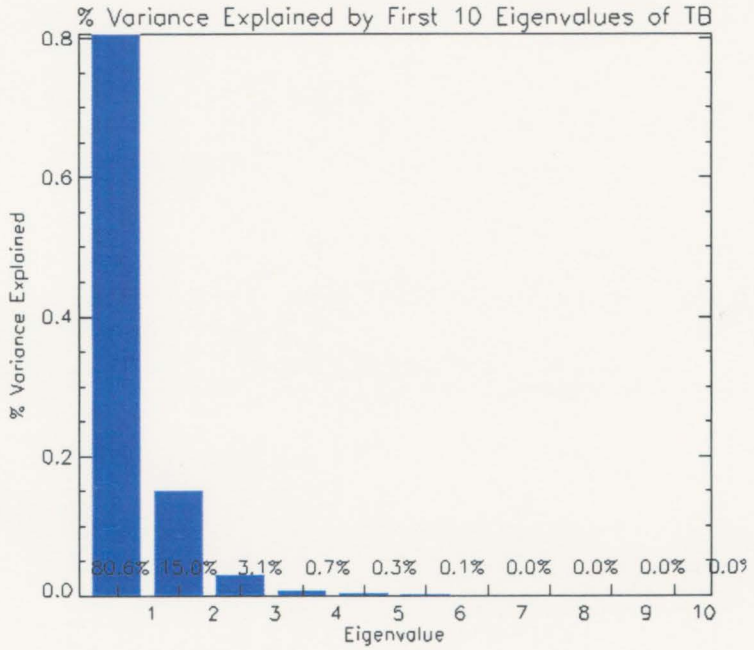

Fire 4.04

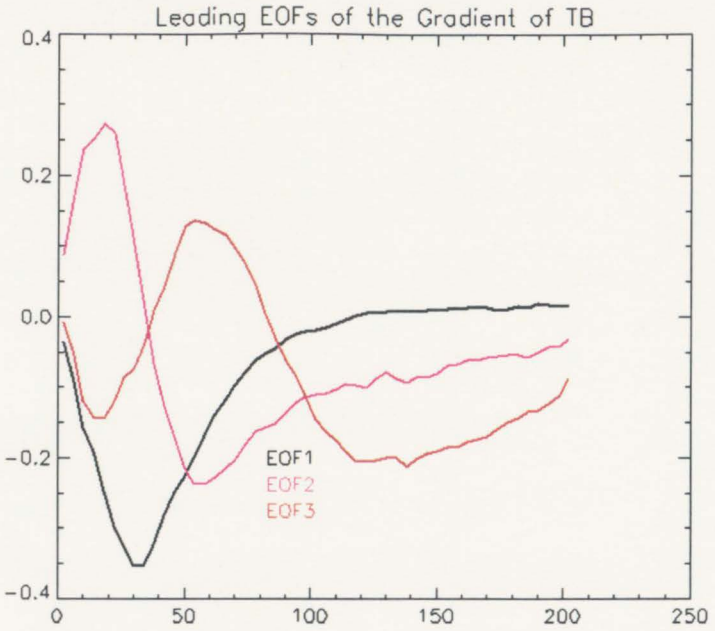

Figure 4.05

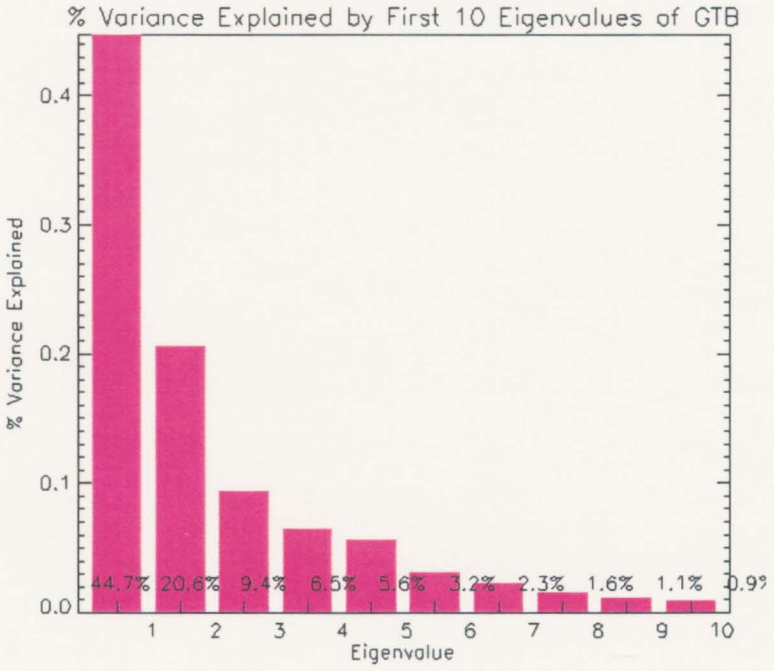

Figure 4.06

4.2 STATISTICAL METHODS

4.2.1 Radius of Maximum Wind Prediction Equation:

Theoretically, every predictor discussed in the previous section is physically relevant to the radius of maximum wind in a tropical cyclone, however the specific significance of any particular variable is unclear. Hence, the relationship between the predictors and the predictand is analyzed using a multiple linear regression technique. Conventionally, y is the symbol for the dependent variable, or predictand, and x_i is the symbol for the independent variables, or predictors, where i = 1, 2, ……., K. For a given data set with K predictors, the predictive equation is of the form:

$$y = b_0 + b_1 x_1 + b_2 x_2 + . + b_K x_K \qquad [4.1]$$

where b_0 is the constant of fit, and $b_1, b_2 \ldots, b_K$ are the regression coefficients. The regression procedure chooses the constant and coefficients of the line such that there is minimal error in estimations of y given actual observation x_i. Most commonly, this is measured by minimizing the sum of the squared error, hence, it is referred to as a least squares regression. The error, or residual, is simply the difference between the observed and predicted data, defined as,

$$E_i = o_i - y\,(x_i) \qquad [4.2]$$

Generally, it is not necessary, or valuable, to include every possible predictor in the regression equation. Some variables may not be significantly correlated with the predictand, while other predictors may be correlated with each other, thus not adding any additional information to the multiple regression. Therefore, in order to choose the best predictors, several steps must be undertaken. First, each predictor was individually correlated with the predictor, the radius of maximum winds. Highly correlated

predictors, with t-test scores above 98% significance level, were initially accepted into the regression equation. See Figures 4.07 through 4.11 for individual predictor and predictand correlations. At this point, each predictor was tested against all others in order to determine redundancy. In cases of highly correlated predictors, the predictor with the highest correlation to the radius of maximum winds was retained, and all others excluded from the regression.

In the end, five predictors were retained in the linear regression using the radius of maximum wind as the predictand. The list of predictors for RMAX is as follows:

MXWND:	Maximum Azimuthally Averaged Wind Speed
CLD50:	Percent of Pixels Colder Than –50 C^o
PC1TB:	Leading PC of Cloud Top Brightness Temperature
PC3TB:	Third Leading PC of Cloud Top Brightness Temperature
CLDTB:	Radius of Coldest Cloud Top Brightness Temperature

The resulting regression equation for predicting the radius of maximum winds is as follows:

$$PRMAX = 177.5 + (-0.3)MXWND + (-0.8)CLD50 + (305.9)PC1TB + (210.1)PC3TB + (0.69)COLDTB \quad [4.3]$$

The regression equation indicates that as the maximum wind speed in the storm increases, the radius of maximum winds decreases slightly. Similarly, as the percentage of pixels colder than –50 degrees C increases, the radius of maximum winds shrinks. Figure 4.07 and 4.08 illustrate these inverse relationships. There is a positive correlation, however,

between PRMAX and PC1TB, PC3TB, and COLDTB. Figures 4.09, 4.10, and 4.11 illustrate these relationships. PC1TB is related to the mean cold cloud shield, as described previously, therefore the regression relationship suggests that the colder the mean cold cloud shield, the larger the storm, hence the large the radius of maximum winds. Additionally, PC3TB appears to be related to the spiral banding features. As the convective activity in the spiral bands increases, the storm size increases, thus the radius of maximum will be larger. Finally, the colder the coldest radius, the more intense the storm, thus the smaller the radius of maximum winds.

The correlation coefficient between the predicted radius of maximum wind and the observed radius of maximum wind is .577, meaning 34% of the variance is explained. Please see figure 4.12, a scatterplot of prmax and rmax. The solid blue line corresponds to a perfect correlation between RMAX and PRMAX.

Willoughby and Rahn developed a similar empirically determined equation for RMAX (Willoughly, Rahn, 2003) as a function of only the maximum wind and latitude. Their equation is as follows:

$$WRMAX = 46.29\exp[(-0.0153)MXWND + (0.0166)LAT] \qquad [4.4]$$

The exponential in the equation for WRMAX arises because its distribution function has a long tail on the large WRMAX side so that it is more nearly lognormal than normal. Using the Willoughby equation, a prediction for WRMAX was computed for the same cases as were used to calculate PRMAX via the IR technique. A scatterplot of the aircraft observed radii of max winds is plotted against the Willoughby results, with a line

drawn in illustrating a perfect correlation (see Figure 4.13). The r^2 value for the Willoughby predictions is 19.7%, a deterioration on the IR predictions, which had an r^2 of 33.4%. In fact, the Willoughby algorithm tends to highly under-predict RMAX. It is clear from these results that the addition of satellite data to the prediction equation significantly improves the estimations of RMAX in tropical cyclones. It is important to note that the IR algorithm was developed directly from the aircraft data set, while the Willoughby method was derived independent of the aircraft data used in this study, therefore one would expect the IR method to be slightly better.

The RMAX residuals are shown in figure 4.14. Recall that the residuals are calculated by subtracting the aircraft observed values from the IR predicted values. Therefore, positive residuals correspond to an over-prediction, and negative values correspond to an under-prediction. The majority of the predicted values fall between –10 and +10 nautical miles of the observed values, with more cases being over-predicted than under-predicted. In fact, 142 cases are over-predicted using the IR derived algorithm, while only 107 are under-predicted. The scatterplot (Figure 4.12) illustrates that the over-prediction tends to occur at smaller radii, while there is a slight tendency for the IR prediction equation to under estimate at larger radii.

To determine the significance of the relationship between the PRMAX and RMAX, several goodness-of-fit measures are employed. The first measure, the mean-squared error (MSE) is the average of the squared differences between the predicted and observed values.

$$\mathrm{MSE} = \frac{1}{n}\sum_{k=1}^{n}(y_k - o_k)^2 \qquad [4.5]$$

It is an indication of the variability of the quantity being forecast around the forecast regression line, thus the smaller MSE, the better the fit. However, since the MSE is computed by squaring estimation errors, it is especially sensitive to cases with large errors. The root-mean squared error (RMSE) is simply a square root of the MSE, and is used as an estimation of accuracy.

A second indication of the goodness of fit of the regression is the mean absolute error (MAE), which is the average of the absolute values of the differences between the predicted and observed values.

$$\text{MAE} = \frac{1}{n}\sum_{k=1}^{n}\left|y_k - o_k\right| \qquad [4.6]$$

The MAE is a typical measure for predicted errors in a given verification data set.

The MAE for RMAX is 27.8 km. The RMSE is 36 km. These numbers indicate an adequate, but not necessarily robust goodness-of-fit.

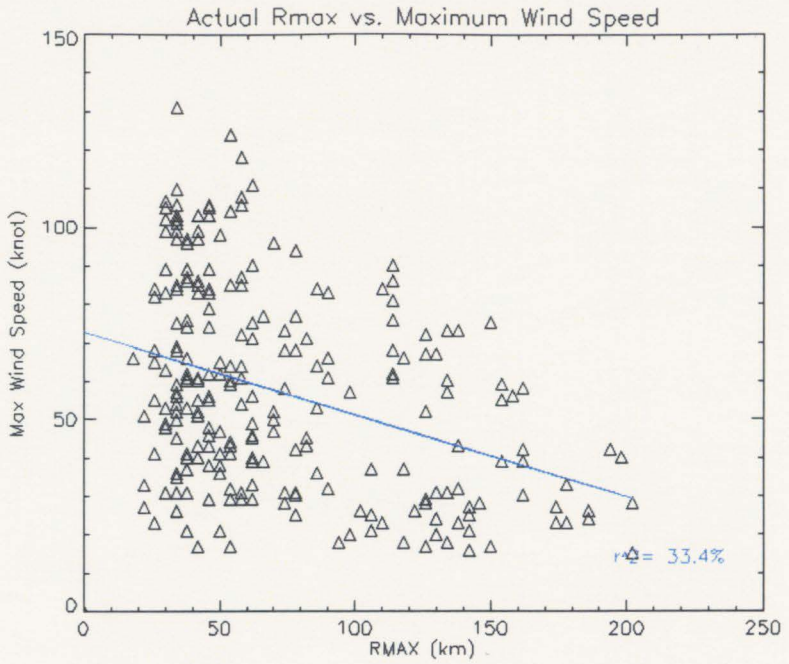

Figure 4.07

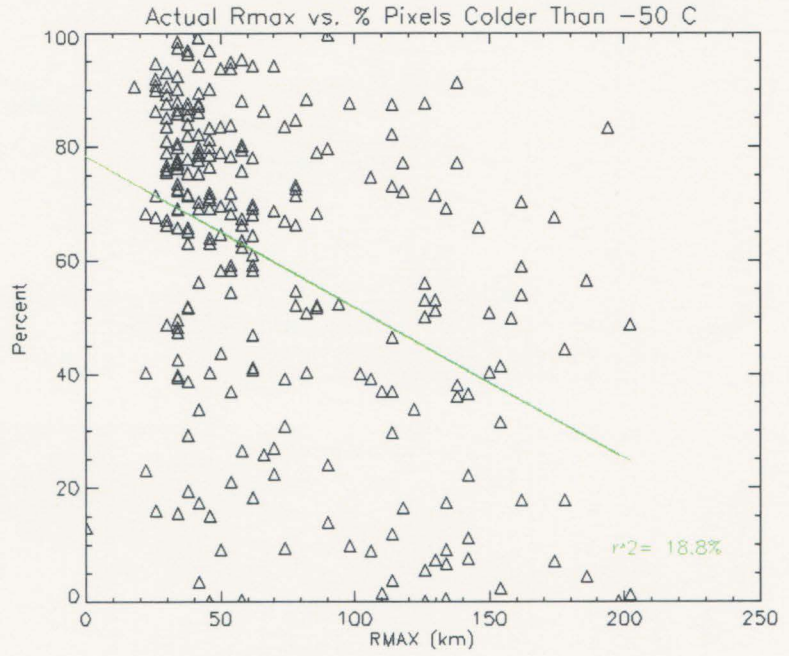

Figure 4.08

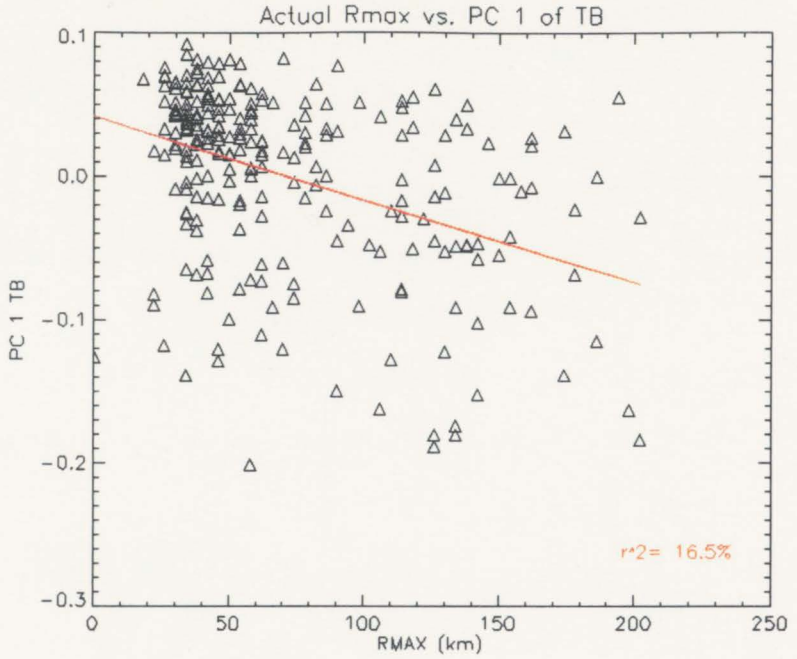

Figure 4.09

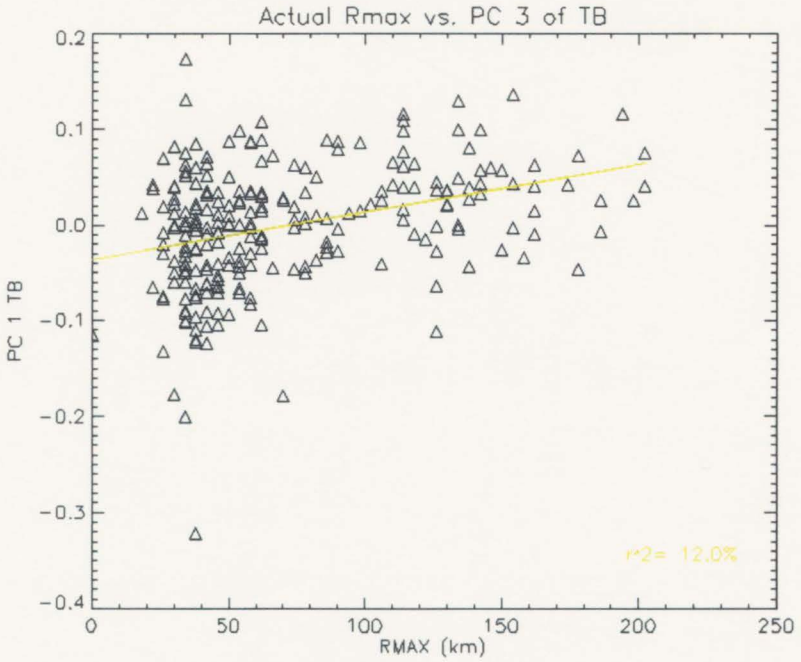

Figure 4.10

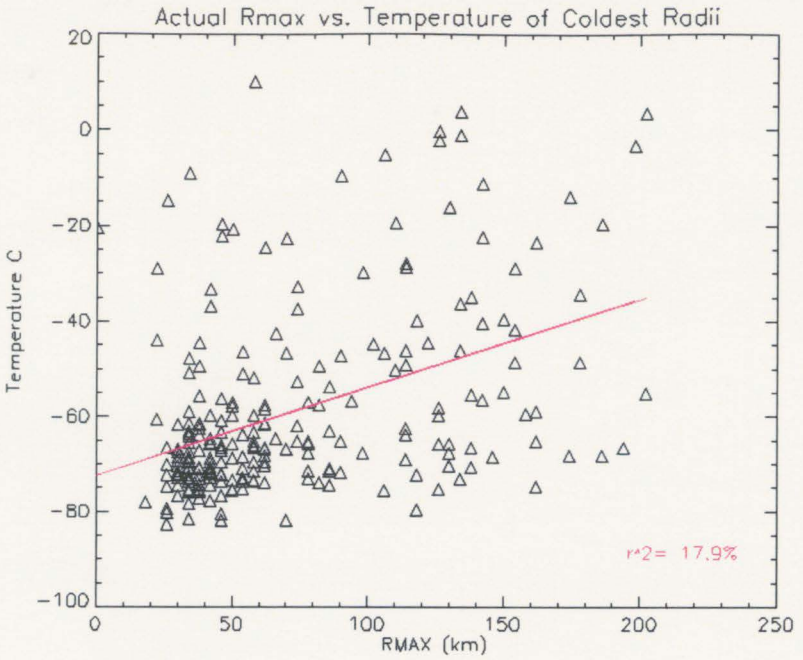

Figure 4.11

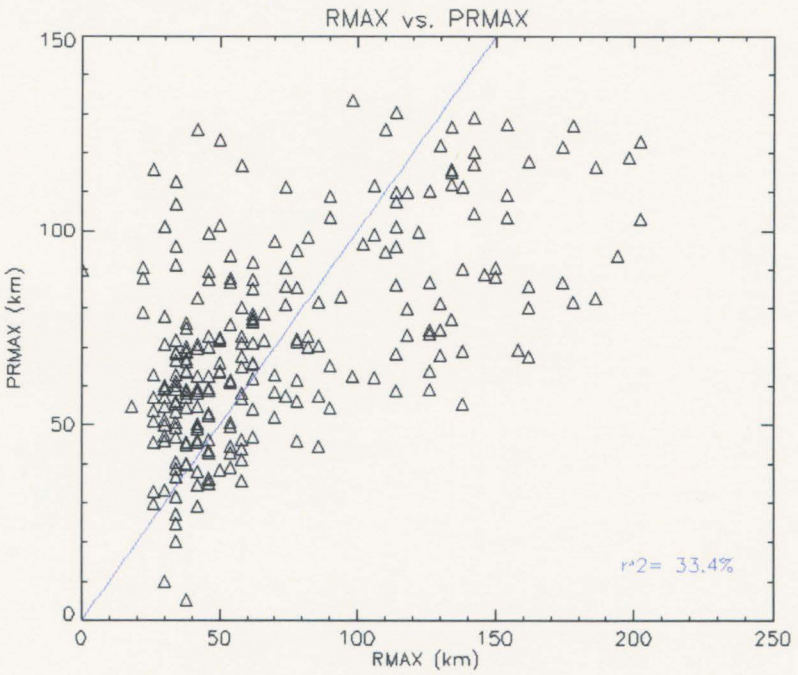

Figure 4.12

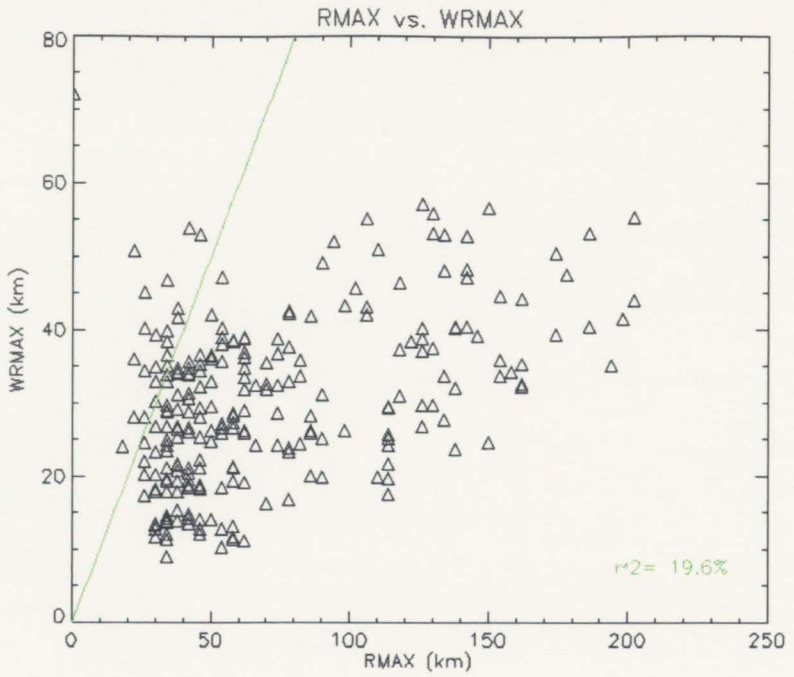

Figure 4.13

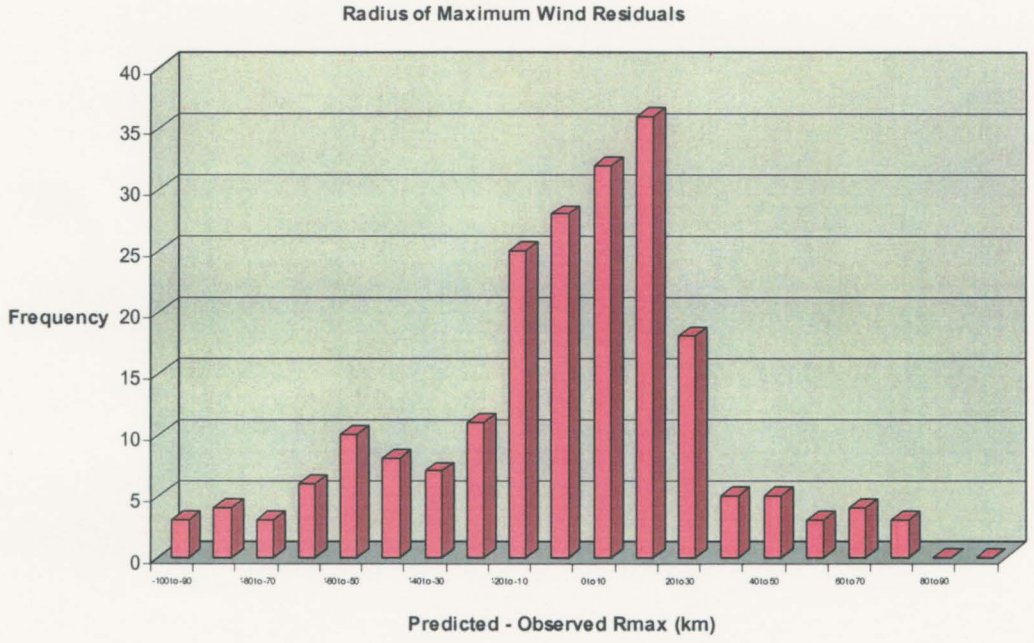

Figure 4.14

4.2.2 PV202 Prediction Equation

Next a linear regression was done using the wind speed at a radius of 202 km as the predictand. The wind speed at a radius of 202 km will serve as a proxy for the storm size. In this case, only four predictors were retained in the linear regression and are listed as follows:

MXWND:	Maximum Azimuthally Averaged Wind Speed
PC2TB:	Second Leading PC of Cloud Top Brightness Temperature
PC2GTB:	Second Leading PC of the Gradiant of Cloud Top Brightness Temperature
LAT:	Latitude of the Storm Center

The resulting regression equation for predicting the wind speed at a radius of 202 km is as follows:

$$PV202 = -8.8 + (0.5)MXWND + (31.9)PC2TB + (-58.05)PC2GTB + (.54)LAT \quad [4.7]$$

The regression equation predicts a positive correlation between the maximum wind and the wind speed at a radius of 202 km (see Figure 4.15). This is plausible physically, because if the wind speed at the radius of maximum winds is quite large, and this wind speed drops off at a predictable rate away from RMAX, then the wind speed at V202 should also be quite large. Next, PC2TB seems to be a manifestation of the size of the cold cloud shield. Figure 4.16 illustrates the fact that if the cold cloud shield grows, it is an indication that the storm is growing in size. This will obviously be directly related to

the winds at a radius of 202km, which is effectively a size parameter. There is also a direct relationship between latitude and the predicted V202 (see Figure 4.18). As a storm moves north, away from the equator, it will typically grow larger. This is consistent with previous studies (e.g. Merrill, 1988)

The inverse relationship between PC2GTB and the predicted V202 is a little harder to understand. As explained above, PC2GTB appears to be capturing the eyewall convection, and the rate at which the convection drops off after this maximum. If the convection drops off rapidly, the storm is likely to be smaller, thus V202 will be smaller. Conversely, if the convection (ie cold cloud top temperature) decreases slowly away from the eyewall, the storm will likely be larger, thus V202 will be greater.

The correlation coefficient between the predicted wind at r=202km and the observed wind at r=202km is .807, and 65% of the variance is explained. See figure 4.19, a scatterplot of the predicted versus the observed size parameter values. The solid red line represents a perfect correlation between V202 and PV202. One can see that the prediction equation is quite robust, as the fit is good, and the scatter is minimal.

The V202 residual plots indicate that nearly 75% of the cases fall between +10 and –10 knots of the actual wind speed at a radius of 202 km (Figure 4.20). It appears that there is a randomness to the over or under prediction in terms of the size of the storm. The goodness-of-fit tests indicate that the IR V202 prediction equation is much more robust than the IR RMAX prediction equation. The MSE is 7.8 kt, and the RMSE is 9.6 kt.

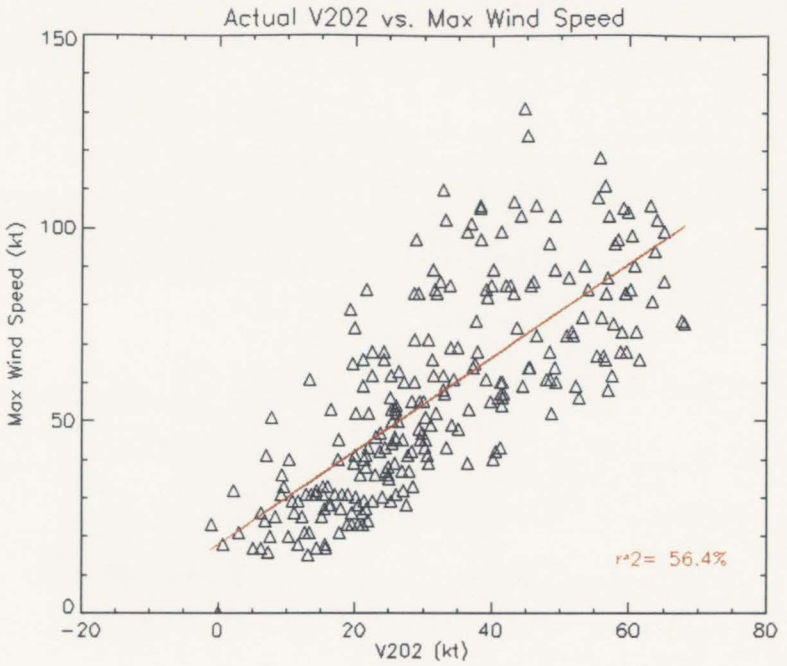

Figure 4.15

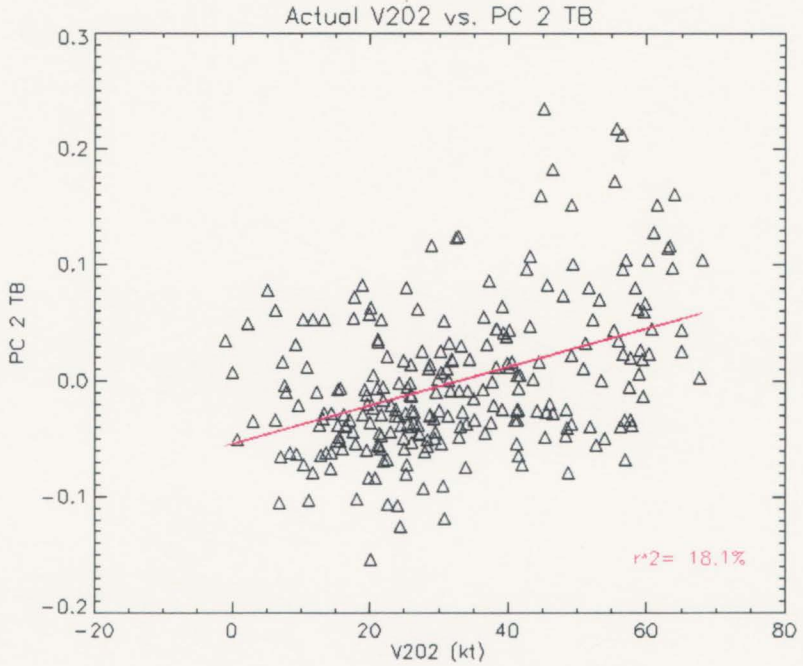

Figure 4.16

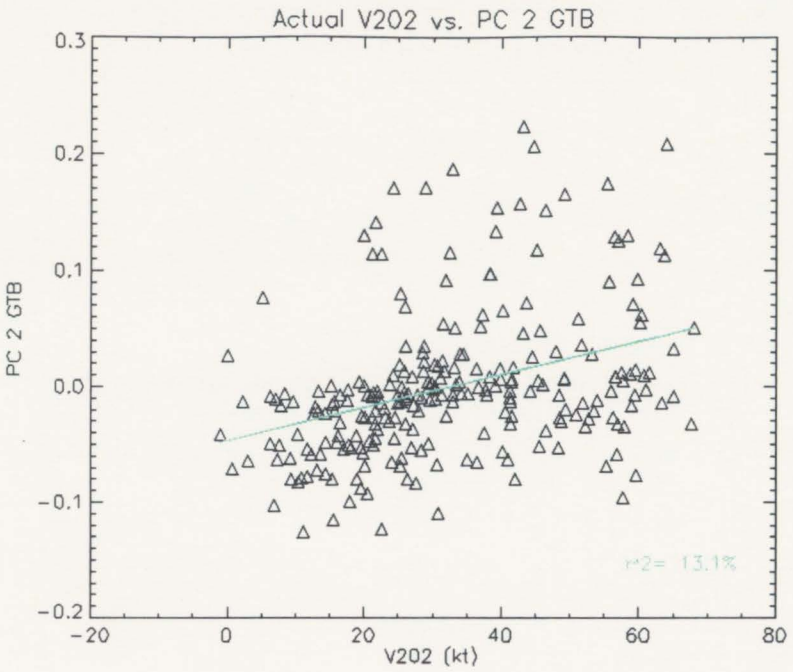

Figure 4.17

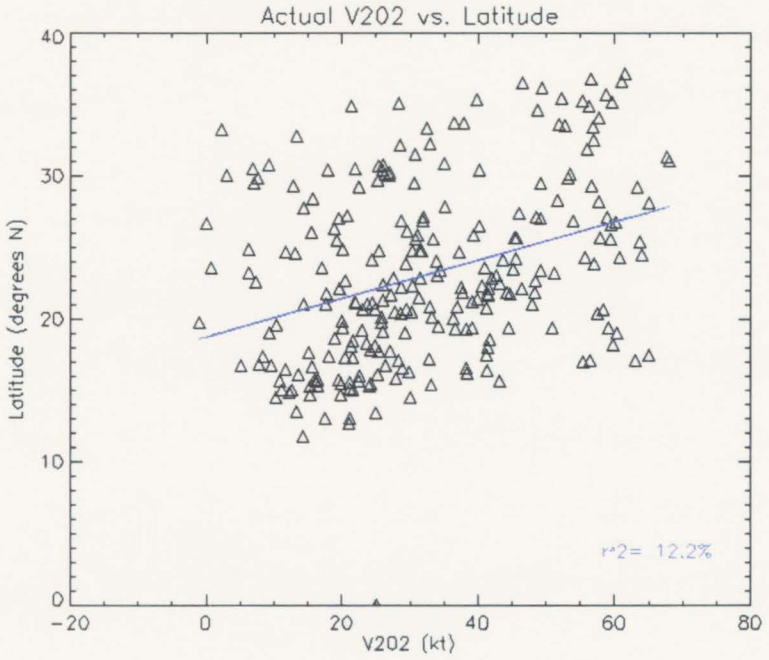

Figure 4.18

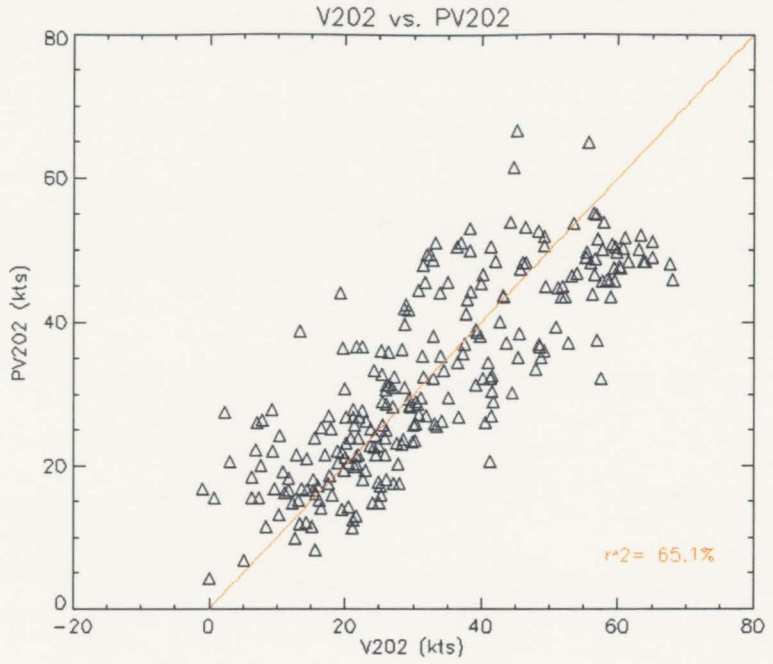

Figure 4.19

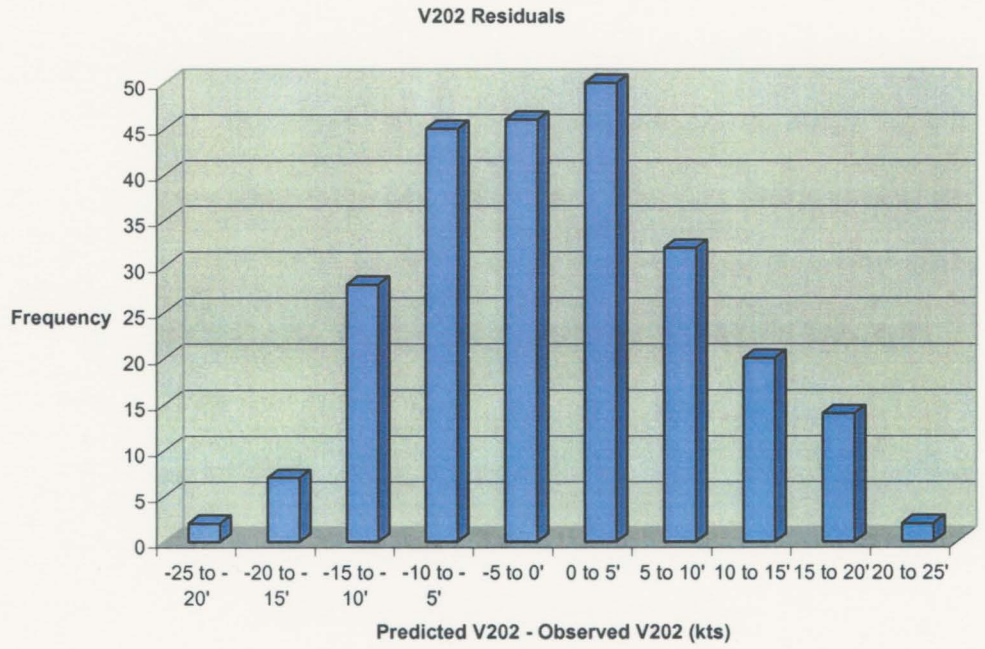

Figure 4.20

Table 4.1

	MAE	RMSE
RMAX	27.8	36
V202	7.8	9.6
Azimuthally Averaged Wind Field	7.56	10.2

4.2.3 Symmetric Wind Field Prediction

Once the parameters RMAX and V202 are estimated, the next step is to estimate the entire symmetric wind field. As Holland (1980) suggests, a valid method of using sparse observations to provide objective estimates of destructive wind extent in a tropical cyclone is with an analytical model of hurricane wind profiles. The Rankine Vortex is a simple vortex model, often called a Rankine combined vortex for the reason that it is built from two separate two dimensional flow fields. The interior flow field is one that has only a tangential velocity, which increases linearly from zero along the central axis to a maximum value at a radius R_m. This interior region rotates like a solid body, with constant vorticity, even though it is fluid:

$$V/r = \text{constant}$$

The outer flow is also purely tangential and begins with its maximum velocity at radius R_m. The velocity in this outer region is inversely proportional to the distance from the origin:

$$Vr = \text{constant}$$

In this study, a modified Rankine Vortex is considered, where the tangential wind is given by:

Vr^x = constant

Thus, the modified Rankine vortex is described by

$$V(r) = V_m(\frac{r}{R_m}) \qquad r < R_m$$
$$V(r) = V_m(\frac{R_m}{r})^x \qquad r > R_m \qquad [4.8]$$

Where V = tangential wind speed, V_m = maximum tangential wind speed, r = radial coordinate and R_m = radius of maximum wind, and x is unitless, positive number derived empirically from existing infrared data. An exponent of unity would signify the assumption of conservation of angular momentum, and solid body rotation. According to Holland (1980), the value of x outside the radius of maximum wind is less than unity and it usually lies between 0.4 and 0.6, although it can be lower or higher. These flatter profiles in the outer radii are a manifestation of the loss of angular momentum experienced by inflowing air parcels due to friction and convective processes. Although the model is highly simplified, and in actually, a Rankine vortex cannot be exactly reproduced in the atmosphere, it is often used as a model for the wind distribution in a TC. Figure 4.21 is an example of a modified Rankine tangential wind profile of a hypothetical tropical cyclone with a maximum wind speed at 100 kts, an RMAX of 55 km, and x set to 0.5.

An important thing to note when using a Rankine Vortex is that the entire symmetric wind field is represented by only tangential wind. The radial symmetric wind field is neglected in the Rankine Vortex. This assumption is valid according to calculations performed on the actual aircraft data. The symmetric radial wind calculated

at each radius is approximately zero (mean of -.72 knots), and is negligible compared to the symmetric tangential wind at each radius (mean of 40.4 knots). See Figures 4.22 and 4.23. Note the scale difference between the radial and tangential mean symmetric wind fields. Also observe that the mean tangential wind profile from aircraft data is quite closely approximated by a Rankine vortex model, while the radial wind profile has an entirely different shape. Since the aircraft is typically measuring the winds at 700 mb, the radial wind is quite small and can be neglected in the symmetric mean. If the aircraft were measuring wind speeds near the surface, the radial wind would have a larger negative component due to friction. In chapter 6, the asymmetric wind field will be approximated by the storm motion vector, and the radial wind component will no longer be neglected. For the time being, we will assume that the symmetric tangential wind field is highly representative of the actual flow field in a hurricane.

The regression method described above is used to predict a radius of maximum wind and a wind speed at a radius of 202 km, from various known parameters including infrared BT data and latitude. A maximum wind speed can be calculated using the Dvorak technique from the same infrared data. Therefore, in (4.8), V_m and r_m are known, and x can be determined so that V at r=202 km matches the predicted value. This exponent will be different for each storm case. Once, V_m, r_m, and x are known, (4.8) can be used to estimate the entire symmetric wind field.

4.3 RESULTS

Figure 4.24 shows the distribution of the correlation coefficient between the predicted symmetric, tangential wind field and the actual symmetric, tangential wind

field as measured by aircraft for each case. 210 of the 249 cases exhibit overall correlations of better than .50, and nearly 90 cases exhibit excellent correlations of greater than .90. These results are promising and interesting alone, however, the next step is to determine which cases are performing well, and which are performing poorly, in terms of radius of maximum wind, maximum wind speed, and storm size.

Figure 4.25 is a plot of the mean maximum wind speed for all cases with a correlation coefficient above a certain threshold, beginning with all cases on the far left, and ending with only those cases with a correlation greater than .98 on the far right. One can see that the mean MAXWND for all 249 cases is near 57 kts. As the cases with lower correlation coefficients are left out of the calculation of the mean max wind speed, the mean MAXWND increases. The mean MAXWND for cases with a correlation of better than .98 is 81 kts. As further evidence, there are 22 cases in which the correlation between the predicted and actual wind fields is greater then .97, and the mean MAXWND for these high performance cases is 78 kts. Similarly, there are 22 cases in which the correlation coefficient between the predicted and actual wind fields is less than .40, and the mean MAXWND for these low performance cases is only 40 kts. Thus, there is nearly a 40 kt wind speed difference between the 22 worst performing cases and the 22 best performing cases. Thus, cases in which the maximum wind speed is greater perform significantly better than cases in which the mean MAXWND is quite weak. Physically this is reasonable because more intense storms tend to be better organized, thus they are structured in a manner than is easier to predict from IR data.

Figure 4.26 is a similar plot, however in this case, a mean radius of maximum winds is calculated for all cases with a correlation coefficient greater then certain

thresholds, again from .00 to .98 and above. The relationship is not quite as robust as the relationship described between the mean max wind speed and performance, however, it is clear that cases in which the correlation is higher do tend to exhibit a larger RMAX. The mean RMAX for all cases is near 72 km, whereas the mean RMAX for cases with a correlation of .90 or better is approximately 78 km. It is therefore likely the storms with a larger RMAX tend to perform slightly better than small RMAX storms. Perhaps a better measure of this assertion is to compare the best 22 cases to the worst 22 cases, in the same manner as described above. The 22 best performing storms (those with a correlation coefficient greater than .97) exhibit a mean RMAX of 82.9 km. Conversely, the 22 worst performing cases (those with a correlation coefficient of less than .40) exhibit a mean RMAX of only 31.3 km. There is greater than a 50 km difference between the best and worst performing cases, thus, the evidence clearly supports the assertion that storms with a larger RMAX do perform better in the Rankine Vortex model.

A final means of stratifying the cases is to calculate the mean wind speed at a radius of 202 km, a proxy for the storm size. Figure 4.27 illustrates that the mean V202 for all 249 cases is approximately 33 kts, while the mean V202 for all cases with a correlation coefficient of .98 or better is 50 kts, a significant difference. Again, the best and worst cases were compared, resulting in a 30 kt difference between the best and worst performing cases. Thus, one can speculate with confidence that larger storms tend to perform better in the Rankine Vortex model.

From this stratification analysis, it is clear that larger, stronger storms tend to be easier to recreate in terms of the symmetric tangential wind field via a regression

technique and the use of a Rankine Vortex model. Not surprisingly, these storms perform better because they have a structure that is more organized, and predictable using a simple model. Weaker, disorganized storms are much harder to recreate from simply an estimation of a radius of maximum winds and a size parameter, because the wind structure is more complicated, and does not follow any sort of model for mature cyclone structure.

Figures 4.28 through 4.33 illustrate both high performance and low performance cases. Figure 4.28 is a plot of the actual wind field against the predicted wind field from Hurricane Felix in the Atlantic in 1995. The red line represents a perfect correlation between the predicted azimuthally averaged, tangential symmetric wind field and the actual wind field as measured by aircraft, for all 51 radii. The diamonds represent the actual correlation. Figure 4.29 contains plots of both the actual and IR predicted wind fields as a function of radius. One can see that this was a very high performance case, however it is not perfect. The model tends to under-predict the wind field, especially outside the radius of maximum winds, however it does an excellent job of reproducing RMAX via the regression technique. Figures 4.30 and 4.31 are the same plots for another high performance case, Dennis in the Atlantic in 1999. Again, the regression technique accurately predicts the radius of maximum winds, and the Rankine Vortex model accurately describes the flow field, especially inside RMAX. An important feature to note is that in both of these high performance cases, the maximum wind speeds are high, 66 kts in the case of Felix, and 77 knots in the case of Dennis.

Conversely, Figures 4.32 and 4.33 illustrate a case that performed very poorly, Edouard in 2002, and in this case the maximum wind speed is only 27 knots, again

emphasizing the higher quality of analysis for bigger, more intense storms. The aircraft observed wind field in Figure 4.33 is highly sporadic, with a pair of weak wind maximums, instead of one prominent RMAX. Thus, the regression technique proved quite unsuccessful at predicting RMAX, and the Rankine Vortex model is unable to resolve two wind maximums. It is increasingly evident that complex, weak, disorganized systems do not perform well using the combined regression Vortex model method.

The same goodness-of-fit tests were applied to the derived wind field as were applied to the predicted radius of maximum wind and the predicted wind speed at a radius of 202 km. The MAE for the wind field for all 249 cases is calculated to be 7.2 kts, and the RMSE is 10.2 kts.

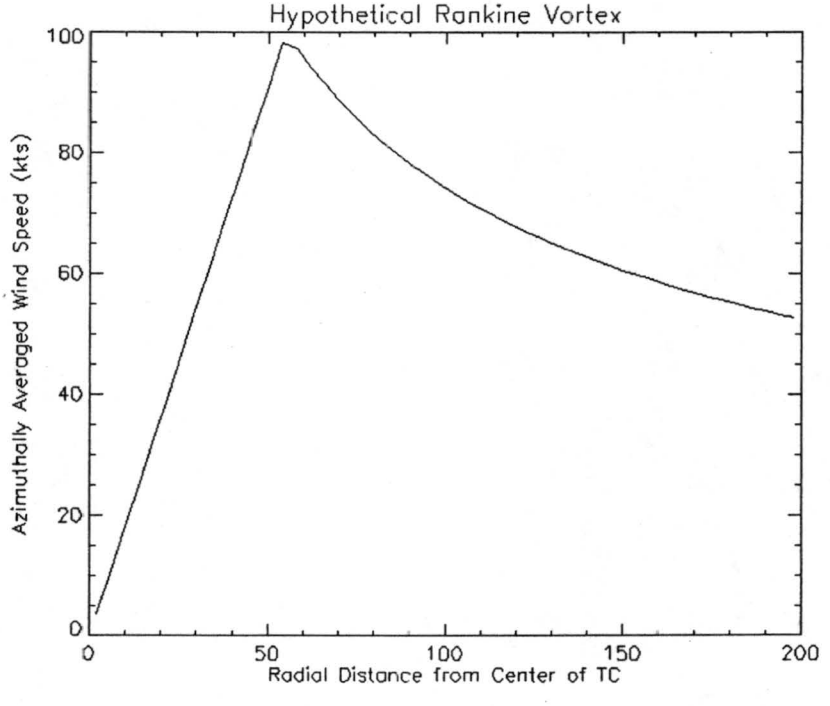

Figure 4.21

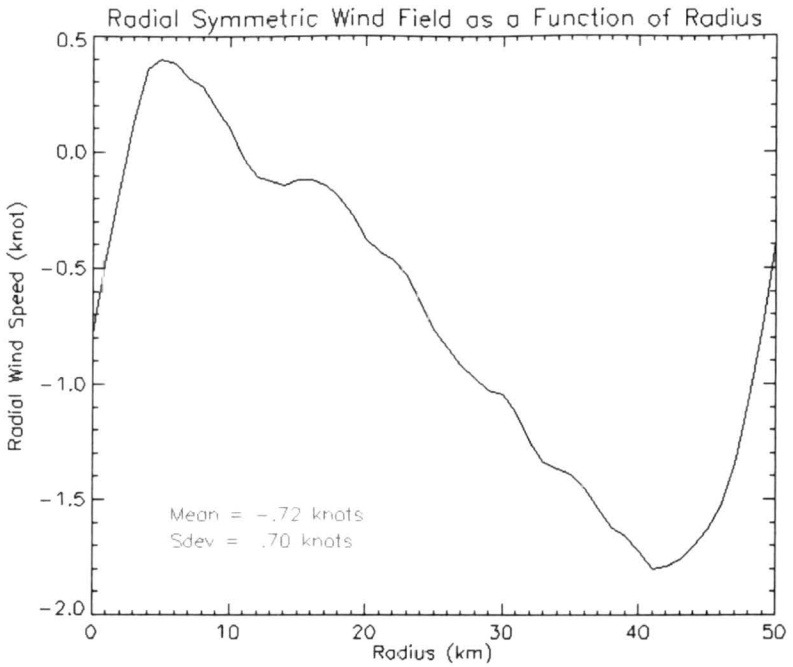

Figure 4.22

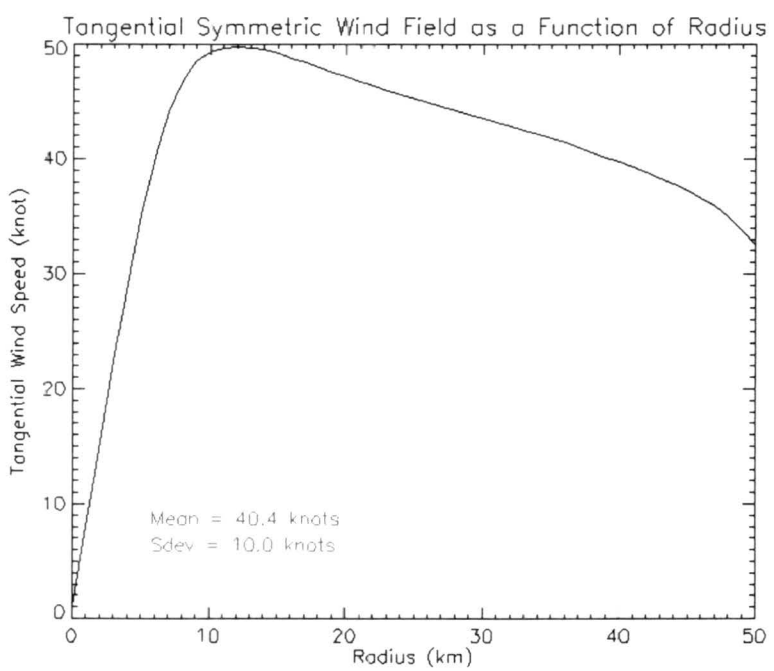

Figure 4.23

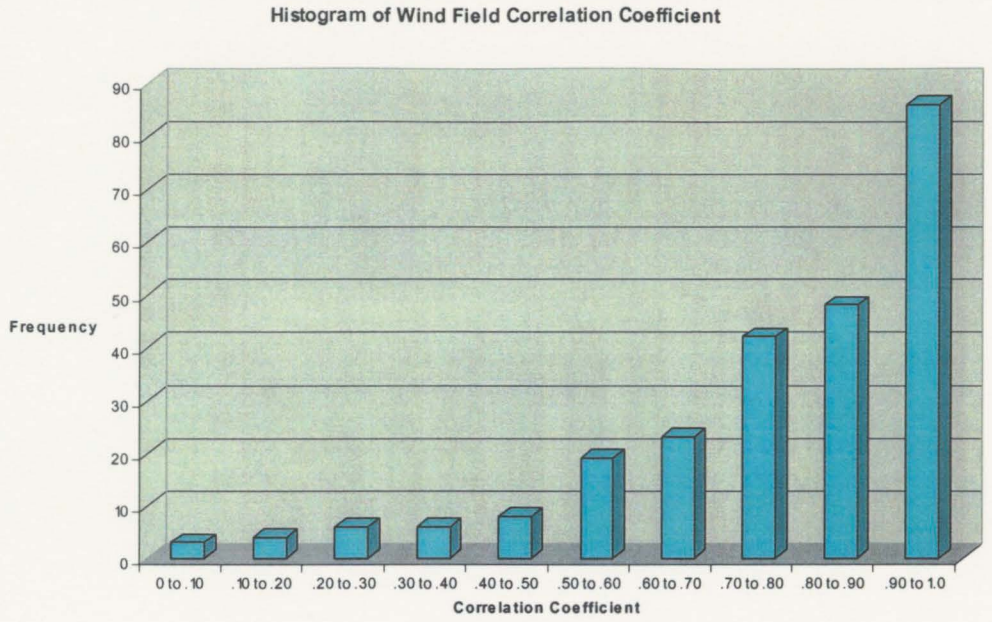

Figure 4.24

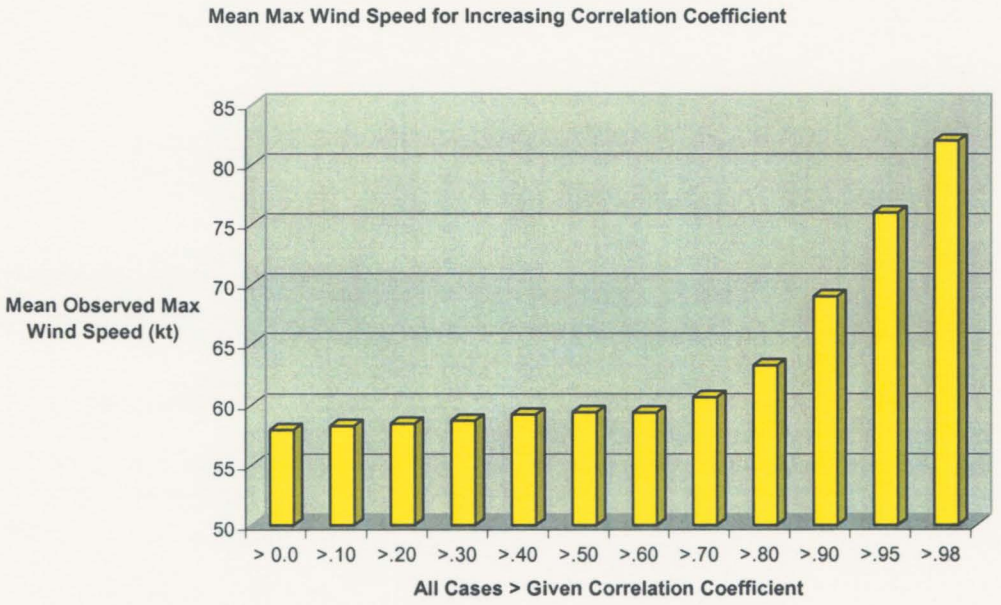

Figure 4.25

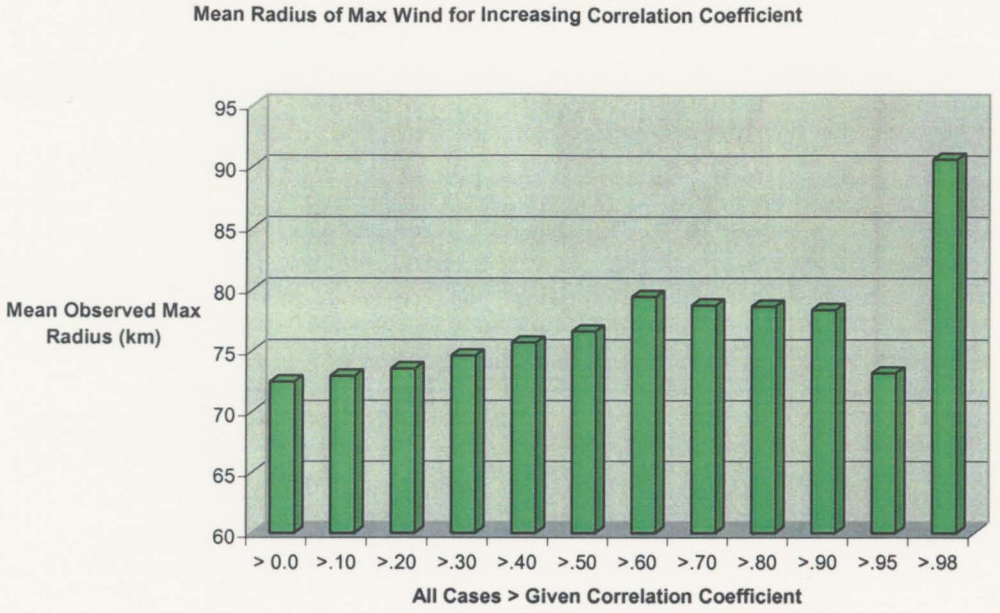

Figure 4.26

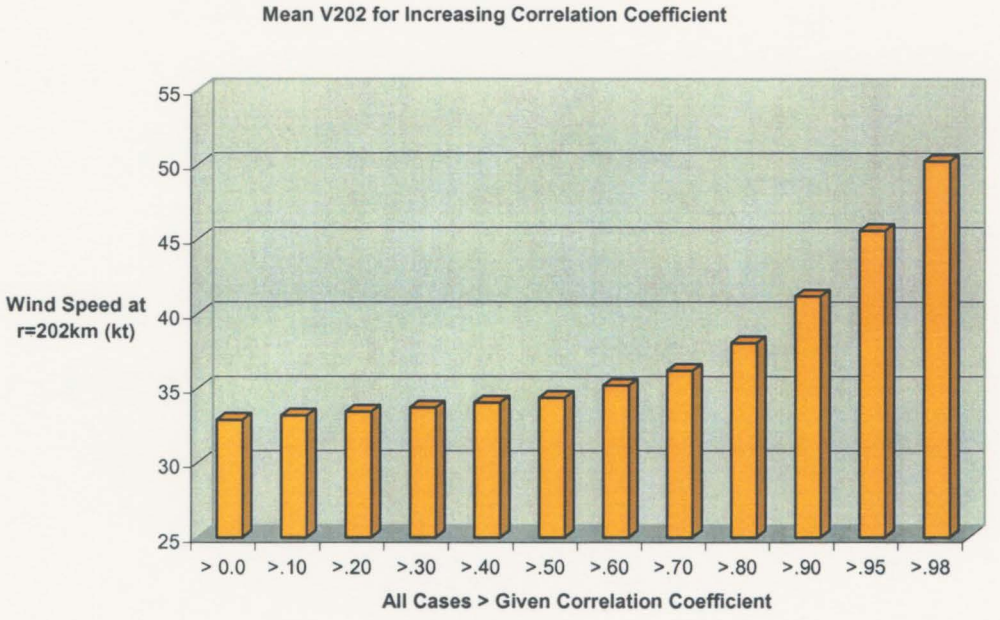

Figure 4.27

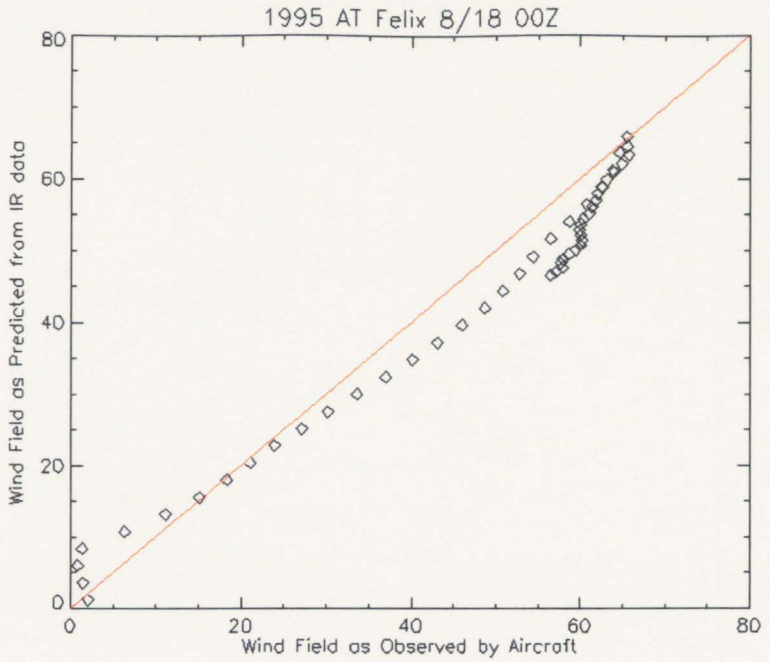

Figure 4.28

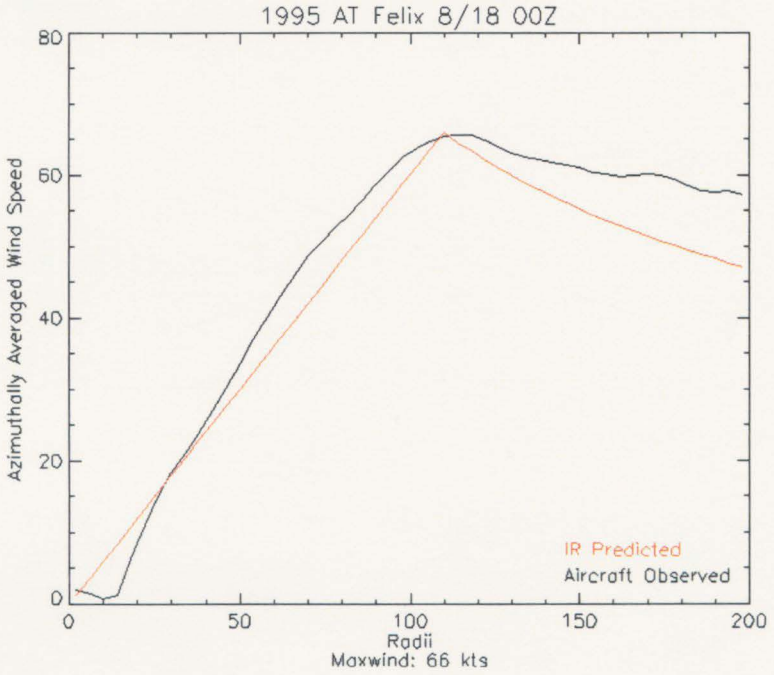

Figure 4.29

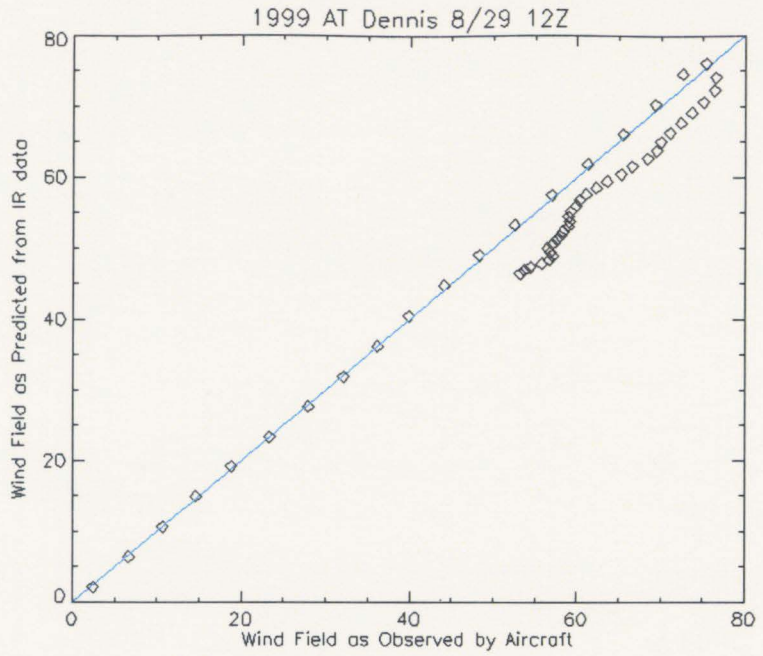

Figure 4.30

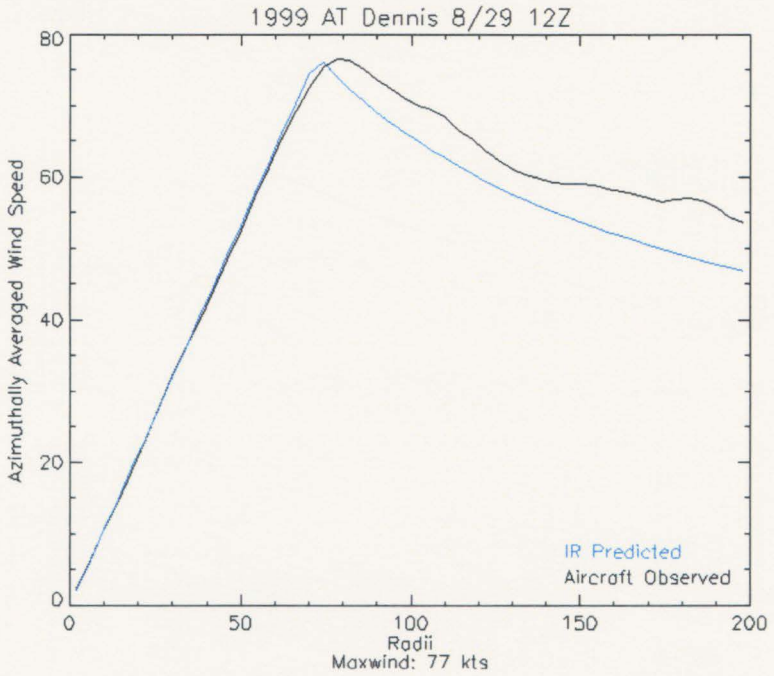

Figure 4.31

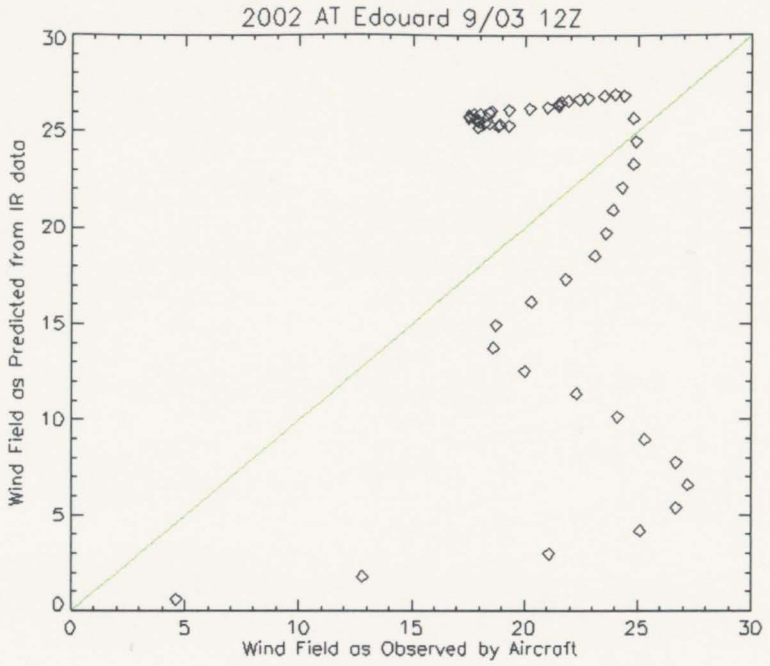

Figure 4.32

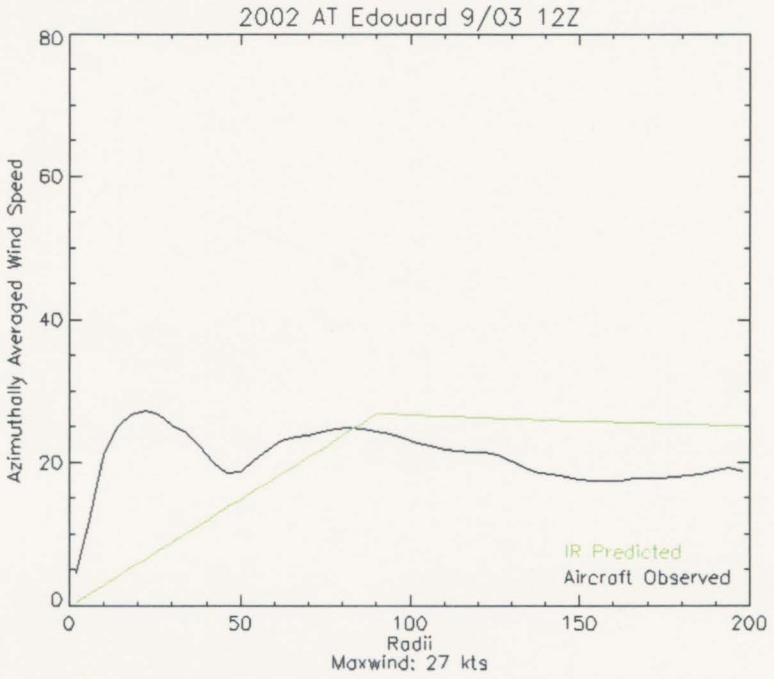

Figure 4.33

CHAPTER 5 – ASYMMETRIC WIND ANALYSIS

Chapter 4 is devoted to describing a technique to recreate the symmetric wind field in a tropical cyclone from infrared satellite data. In this section, a method to add an asymmetric wind component is presented. For the purpose of this analysis, the storm motion will be assumed to be the only contributor to tropical cyclone asymmetry. In reality, there are most likely several parameters that become important factors, such as wind shear over the storm domain. Basically, this portion of research revolves around answering the question of how much asymmetry can be explained by the storm motion alone, and can it be used in conjunction with the symmetric wind analysis to more accurately portray the wind field in a tropical cyclone.

5.1 THE ASYMMETRIC WIND FIELD

The asymmetric wind field is defined to be the difference between the aircraft observed tangential wind at each of 51 points along 16 radial legs in the analysis grid, and the aircraft derived azimuthally averaged wind at each of the 51 radii. The asymmetric wind at each of 16 points in the azimuth, for each radii separately, is then projected onto a sine function using Fourier decomposition. The phase and amplitude of the asymmetric wind field at each radii is then compared to the phase and amplitude of the storm motion vector, also projected onto a sine function. For the purposes of comparing the aircraft data wind asymmetries and the storm motion vector, 322 cases are retained, versus the 249 used for the IR derived symmetric wind field. This is because we are not constraining our analysis cases to matching IR cases.

The principle of Fourier analysis consists of decomposing an arbitrary function $s(t)$, possibly periodic, into simple wave forms, i.e. into a sum of sine and cosine waves in the case of a periodic wave form, and into an integral over sine and cosine waves, if the wave form is not periodic. This way one obtains a representation of the original wave form that allows one to identify easily which frequencies are contained in the wave form.

Let V(θ) be the entire wind field function, defined in the interval (0,2π) and having the period 2 π. The Fourier Series, or Fourier expansion corresponding to V(θ) is defined to be:

$$V(\theta) = b_0 + \sum_{n=1}^{\infty} a_n \sin(n\theta) + \sum_{n=1}^{\infty} b_n \cos(n\theta)$$

Since b_0 is simply the constant term, which is defined as the mean of the function V(θ), we can replace b_0 with V_0, the azimuthally averaged wind speed at a particular radii, and the equation becomes:

$$V(\theta) - V_0 = \sum_{n=1}^{\infty} a_n \sin(n\theta) + \sum_{n=1}^{\infty} b_n \cos(n\theta)$$

where the Fourier Coefficients a_n and b_n are defined as:

$$a_n = \frac{1}{2\pi} \int_0^{2\pi} [V(\theta) - V_o] \sin(n\theta) d\theta$$

$$b_n = \frac{1}{2\pi} \int_0^{2\pi} [V(\theta) - V_o] \cos(n\theta) d\theta$$

The subscript n corresponds to the wave number, or wave form. Wave number zero is the mean flow field, and the higher wave numbers represent the storm asymmetries. In order to simplify the calculations, in can be shown that the wave number one component of the asymmetric wind field captures quite closely the original function. Figure 5.01 illustrates the contributions of higher order wave numbers. The heavy blue line

represents the original tangential asymmetric wind field for a specific case at a specific radii. The x-axis represents a point along each of 16 radial legs, and the y-axis is the amplitude of the function. The red line is the wave #1 contribution to the wind asymmetry. It is already highly representative of the total asymmetry. The orange line is the wave #1 plus the wave #2 contribution, and it is clear that the addition of the wave #2 asymmetry leads to a slightly more accurate approximation of the total function. The addition of wave numbers 3,4 and 5 all bring the representation slightly closer to the original function. If all wave numbers are combined, the exact original function will be recreated. However, because the addition of the higher order wave numbers is only a slight improvement upon the wave #1 approximation, for simplicity, they can be ignored in further calculations. This simplifies our equations to the following:

$$v`(\theta) = v_c(\theta)\cos\theta + v_s(\theta)\sin\theta$$

$$u`(\theta) = u_c(\theta)\cos\theta + u_s(\theta)\sin\theta$$

Figure 5.02 illustrates the wave #1 sine and cosine contributions to the wave #1 asymmetry. Also plotted is the actual tangential wind field asymmetry. In this case, the original tangential wind field asymmetry is closely approximated by the cosine portion of the wave #1 contribution. The addition of the sine contribution brings the solution closer to the actual asymmetry.

The wind asymmetry as a function of radius can also be calculated in terms of phase and amplitude, to later be compared to the phase and amplitude of the storm motion vector. This is done via the following equations:

$$A_v = \sqrt{v_c^{\,2} + v_s^{\,2}}$$

$$A_u = \sqrt{u_c^{\,2} + u_s^{\,2}}$$

where A_v and A_u represent the amplitude of the tangential and radial components of the wave number one wind asymmetry, and

$$\phi_v = \tan^{-1}\left[\frac{v_s}{v_c}\right]$$

$$\phi_u = \tan^{-1}\left[\frac{u_s}{u_c}\right]$$

represent the phase of the tangential and radial components of the wave number one wind asymmetry.

5.2 THE STORM MOTION ASYMMETRY

If it often assumed that tropical cyclone wind asymmetries are due in large part to the motion of the storm itself. If this is true, then by incorporating the storm motion into our analysis, an accurate approximation of the windfield will be possible, both in the symmetric mean, and with asymmetries.

It is necessary first to understand how storm motion asymmetries contribute to the total asymmetry of the storm. It can be theorized that there is a relationship between the phase of the storm motion vector and the phase of the asymmetry. For instance, the storm motion vector may be acting in one direction, but the asymmetry reacts at some lag to that direction. Furthermore, there should be a relationship between the amplitude of the storm motion vector and the amplitude of the asymmetry. Most likely, the storm motion vector contributes to the asymmetry, but because other factors are also probably

affecting the asymmetry (such as wind shear, relative flow field and convective asymmetry), the ratio of amplitudes will not be one.

Data used to calculate a storm motion vector comes from the NHC best track. A storm motion vector is calculated using the latitude and longitude from –12 hours and the 00 hour (analysis time) latitude and longitude, which corresponds to the twelve hour time period used in the complimentary aircraft analysis.

The storm motion vector is calculated in terms of a speed in the both the x and y directions, and an amplitude (A_c)and phase (ϕ_c), in the manner described above. The motion vector is plotted in fourier space versus the wind asymmetries for several cases in Figures 5.03, 5.04, and 5.05. Note in figure 5.03, the storm motion vector quite closely approximates the wind asymmetry, however this is not true for the subsequent cases. In figure 5.04, the amplitude of the motion vector is very small, 0.7 m/s. Thus, it is not contributingly significantly to the wind asymmetry. In figure 5.05, the amplitude of the motion vector is of the same magnitude as the wind asymmetry, however the phase is off by nearly 180 degrees. It is clear that the amplitude and phase relationship between the storm motion vector and wind asymmetry is complicated.

5.2.1 Simple Model

We are now dealing with only 249 cases in which the aircraft analysis has matching infrared data. The first step in calculating the asymmetric wind field is to translate the storm motion vector into a coordinate system that is comparable to the symmetric wind field grid system. Thus, the x and y direction storm motion vector components must be converted to radial and tangential components in the cylindrical coordinate grid system. The first asymmetric wind field calculations are made without

taking into account any phase bias or amplitude ratio relationships. Instead, it is assumed that the storm motion vector is contributing one – to – one to the wind asymmetries via the following relationships:

$$\begin{bmatrix} c_u \\ c_v \end{bmatrix} = \begin{bmatrix} \cos\theta & -\sin\theta \\ \sin\theta & \cos\theta \end{bmatrix} \cdot \begin{bmatrix} c_x \\ c_y \end{bmatrix}$$

Where θ denotes degrees in the azimuth, from zero to 360, at 22.5 degree spacing.

$$V(r,\theta) = A \cdot c_v + V(r)$$

$$U(r,\theta) = A \cdot c_u + U(r)$$

However, because the radial wind is assumed to be zero in the symmetric mean, the radial asymmetric wind field equation simplifies to:

$$U(r,\theta) = A \cdot c_u$$

and A is assumed to be equal to unity. A total asymmetric wind field is calculated using the radial and tangential components.

From these simple equations in which the storm motion vector is simply added to the symmetric wind at each grid point, an entire asymmetric wind field can be estimated and compared to the aircraft data for the same case. A correlation coefficient is calculated for all 249 cases using this method. Figure 5.06 is a plot of the frequency of ranges of correlation coefficient. The mean correlation coefficient between the observed and derived total wind fields for all 249 cases is .652. A significant number of cases are highly correlated, however there are a handful of low, and even negatively correlated cases as well. The RMSE for this model is 13.4 knots (see Table 1).

The IR derived 3D symmetric wind field is not as highly correlated to the aircraft observed total wind field as the IR derived symmetric wind field plus motion vector (see

Figure 5.07). The mean correlation coefficient is .500 for the IR symmetric and aircraft total wind field. This suggests that the addition of a storm motion vector is actually greatly improving the wind field analysis.

While it appears as though the algorithm is performing very well as it is, recall that while the 2D symmetric wind field correlations were quite high for most cases, there were some cases that were very poorly correlated. If a case is already a poor estimate in the symmetric mean, then there is little hope that by adding asymmetry it will become closely correlated to the actual wind field, and in fact it might even move it farther from the truth. As stated before, the IR algorithm for reproducing the symmetric wind field performs poorly on weak, disorganized disturbances, but performs very well on strong, well-organized tropical storms. Figure 5.14 is an illustration of the observed wind field for Dennis in 1999 (a), and the symmetric (b) and asymmetric (c) IR derived wind field analyses. Dennis was a fast moving, 77 knot tropical cyclone, with a pronounced asymmetry. The symmetric wind field analysis (5.14b) is quite unrepresentative of the actual wind field, however, the once the motion vector is added (5.14c), there is a clear asymmetry, of similar magnitude, phase and shape as the actual wind asymmetry (5.14a). Clearly, in this, and many cases of fast moving, medium strength to strong tropical cyclones that performed well in the symmetric wind analysis, the addition of a motion vector is enhancing the wind field re-creation. It is therefore informative to disregard cases that performed poorly in the 2D symmetric wind field analysis, and concentrate on a subset of cases that performed well.

Taking into account only those cases where the symmetric tangential wind field was correlated at .70 or better (176 cases) to the actual symmetric wind field indeed improves the mean correlation coefficient to .741 (see Table 1), and improves the RMSE to only 12.4 knots. The mean maximum wind for this subset of cases is 62 knots, or roughly the designation between a tropical storm and a tropical cyclone. Thus, we are in effect disregarding weak systems. This simple model suggests that the addition of a

storm motion vector improves the wind field analysis quite significantly, especially when only tropical cyclone strength systems are considered.

5.1.2 Adjusted Model

In order to study the relationship in detail, an tangential amplitude ratio and a tangential phase bias are calculated for each radius:

$$A_R(r) = \frac{A_v(r)}{A_c}$$

$$\phi_B(r) = \phi_v(r) - \phi_c$$

The amplitude ratio and phase bias are calculated at each radii for each of 322 cases in which adequate aircraft data is available. $A_R(r)$ and $\phi_B(r)$ are then averaged over each case and plotted as a function of radius in figures 5.06 and 5.07. The cases are also stratified by the amplitude of the storm motion vector. Fast moving storm cases may behave differently than those that are moving quite slowly.

Figure 5.08 is a plot of $\phi_B(r)$. The phase bias differs between slow and fast moving cases. All cases averaged exhibit a mean phase bias of 20 degrees at inner radii, and up to 50 degrees at outer radii. Before studying the stratification by storm motion, it is necessary to mention that the standard deviation of phase bias for all cases is 79 degrees. This is a very large standard deviation given a mean phase bias of only 60 degrees. It can thus be concluded that the phase bias contains large scatter, and a direct relationship based on these biases is not valid. Note that with a phase bias of zero degrees, the maximum positive asymmetry will act 90 degrees to the right of the storm heading.

Figures 5.09 and 5.10 explore the phase bias relationship from an optimization perspective. The mean correlation coefficients for phase biases ($\Delta\phi$) from -90 degrees to +90 degrees, at 10 degree increments, are calculated after adjusting the tangential and radial motion vector components via the following phase adjusted rotation matrix.

$$\begin{bmatrix} c_u \\ c_v \end{bmatrix} = \begin{bmatrix} \cos(\theta - \Delta\phi) & -\sin(\theta - \Delta\phi) \\ \sin(\theta - \Delta\phi) & \cos(\theta - \Delta\phi) \end{bmatrix} \cdot \begin{bmatrix} c_x \\ c_y \end{bmatrix}$$

Note in these figures that the correlation coefficient is optimized at a phase lag of zero degrees. The MSR is also optimized at a phase lag of zero (where the error is the smallest). Therefore, the phase of the storm motion asymmetry will not be adjusted due to a systematic bias.

Figure 5.11 is a plot of $A_R(r)$. Notice the bright blue line illustrates the tangential asymmetry amplitude ratio for only slow moving cases ($A_c < 5.0$ knots). At inner radii, the tangential asymmetry is almost a factor of six times greater than the storm motion, and it asymptotes to a ratio of approximately two. Conversely, the red line illustrates only fast moving cases ($A_c > 10$ knots). The amplitude ratio for the tangential wind asymmetry versus the storm motion asymmetry is close to unity, meaning that the storm motion vector is a full contributor to the wind asymmetry. It is clear that that amplitude of the asymmetric response to the storm motion is a function of the speed of the tropical cyclone motion.

Because the amplitude ratio for slow moving cases is 6, it is tempting to increase the contribution of the storm motion asymmetry in the wind analysis. However, this ratio is most likely due to the fact that the majority of the actual wind asymmetry in slow moving cases comes not from the small motion vector, but from other factors, such as wind shear and convective asymmetries. Thus, it is not valid to simply force the small motion vector asymmetry to contribute significantly.

Thus, in an effort to isolate an effective contribution amplitude, relationships are explored using the same optimization method described above, adjusting A between 0.5 and 1.7 in the following equations to build the asymmetric wind field:

$$V(r,\theta) = A \cdot c_v + V(r)$$

$$U(r,\theta) = A \cdot c_u + U(r)$$

Figures 5.12 and 5.13 illustrate that the correlation coefficient is optimized at a ratio of 1.4, while the MSR is optimized at 1.2, therefore a compromise is met at an amplitude ratio of 1.3. Thus A becomes 1.3 in the above equations.

After running all 249 cases (this number becomes smaller due to the availability of concurrent IR data) with the adjusted amplitude ratio, a new set of statistics is available. The mean correlation coefficient for the adjusted cases is a slight improvement over un-adjusted cases, at .659. The error statistics remain the same, at 13.4 knot RMSE.

Figure 5.15 is an example of an improvement due to the addition of amplitude adjustment. Figure 5.15(a) is the observed wind field for Hurricane Erin. Figure 5.15(b) is the symmetric wind field, and 5.15(c) is the un-adjusted total IR derived wind field. Note that the analysis provides useful information about the location of the maximum positive asymmetry, however, the amplitude of the asymmetry is slightly low. Figure 5.15(d) is the amplitude adjusted wind field, and it is clear that the higher wind speeds in the wind maximum are now resolvable, however the area magnitude is still slightly off. Conversely, the addition of the adjusted wind field can harm the analysis. For instance, referring back to the case of Dennis, Figure 5.14(d) is the amplitude adjusted wind field. Increasing the amplitude of the response to the motion vector degrades the analysis by overestimating the amplitude of the wind asymmetry.

Furthermore, notice that although the correlation coefficient for a given case might seem quite low, between .40 and .60, it does not necessarily mean that the analysis has performed poorly. For example, Figure 5.16 is an example of Hurricane Juliette in the east Pacific. Again, the correlation coefficient between the actual and IR derived total wind fields is quite low, only .547, however the analysis is quite good at predicting the magnitude and phase of the asymmetry. Unfortunately, the Rankine vortex model is unable to resolve the rapid wind speed changes near the tiny eye of Juliette, which is likely causing the correlation coefficient to be smaller. In spite of this drawback, there is clearly valuable information in the IR derived wind analysis.

5.3 CONCLUSIONS

It is clear that questions asked at the beginning of the chapter have been answered. A majority of asymmetry can be explained by storm motion asymmetry for medium to fast moving cases. The storm motion vector for slow moving cases is too small to largely affect the asymmetry, and other factors are most likely playing a larger role. The storm motion asymmetry can effectively be applied to the symmetric wind field derived in chapter four to produce valid and highly informative estimations of the tropical cyclone wind field.

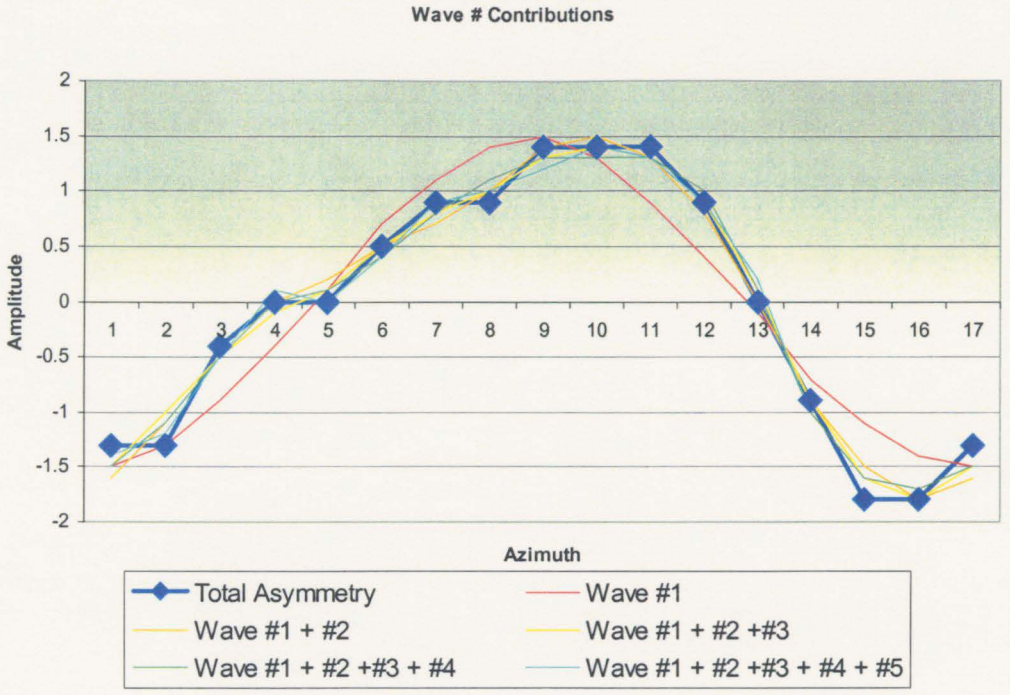

Figure 5.01

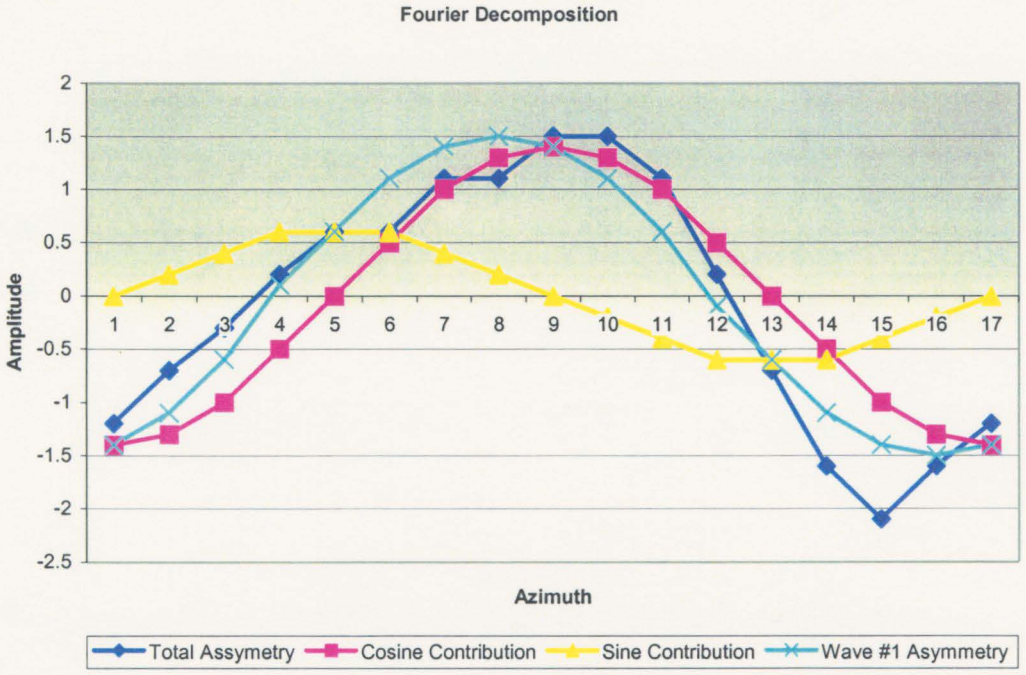

Figure 5.02

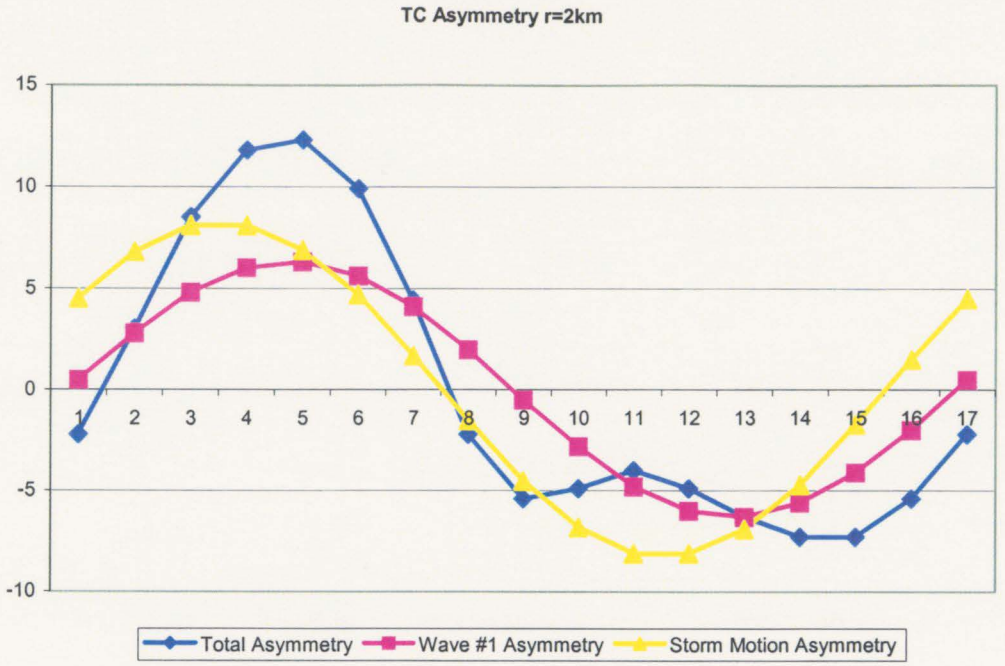

Figure 5.03

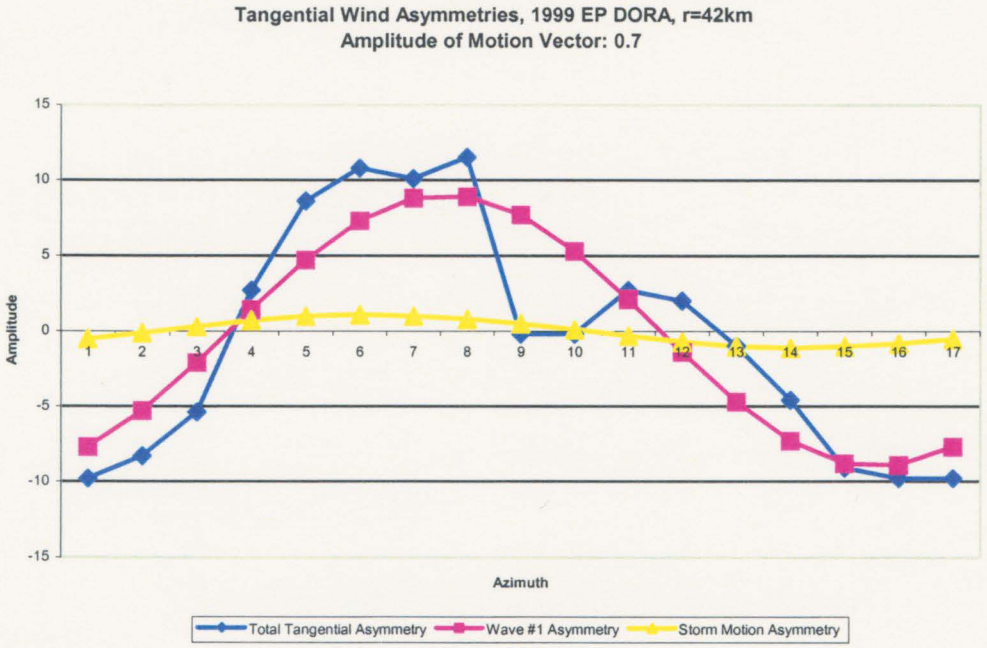

Figure 5.04

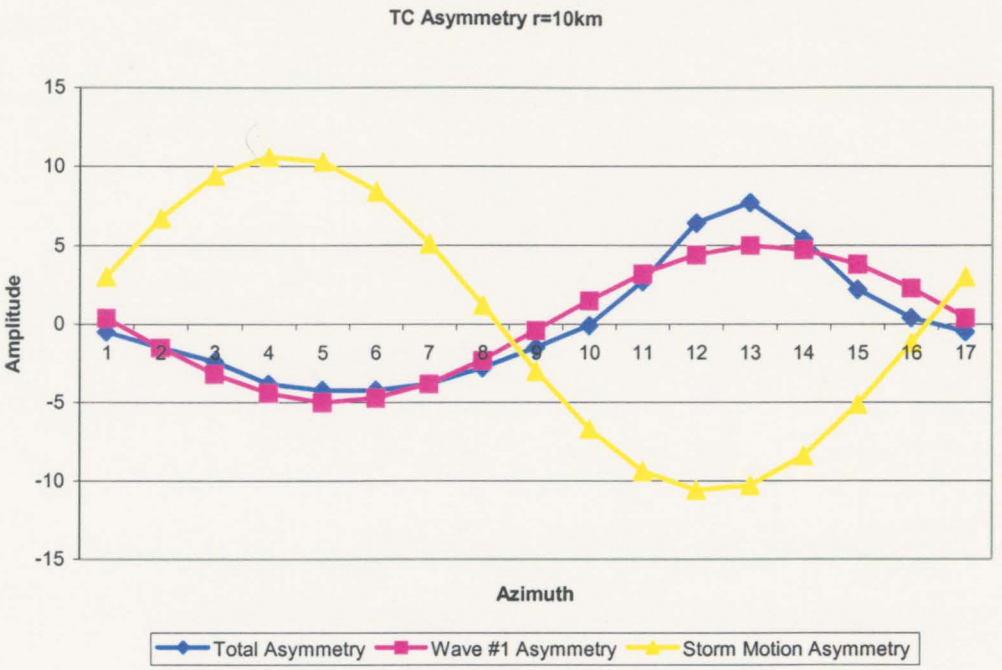

Figure 5.05

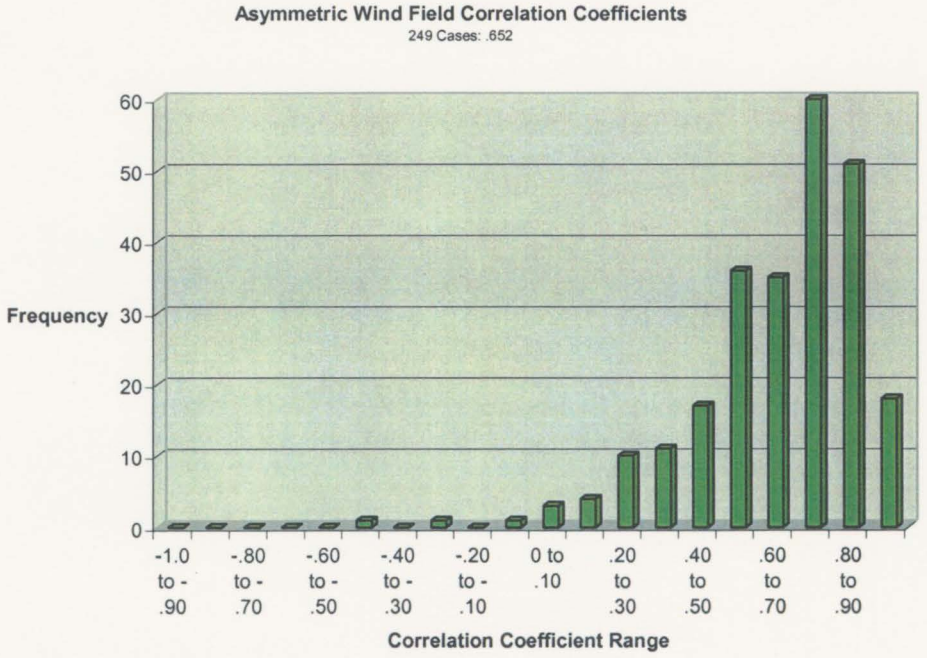

Figure 5.06

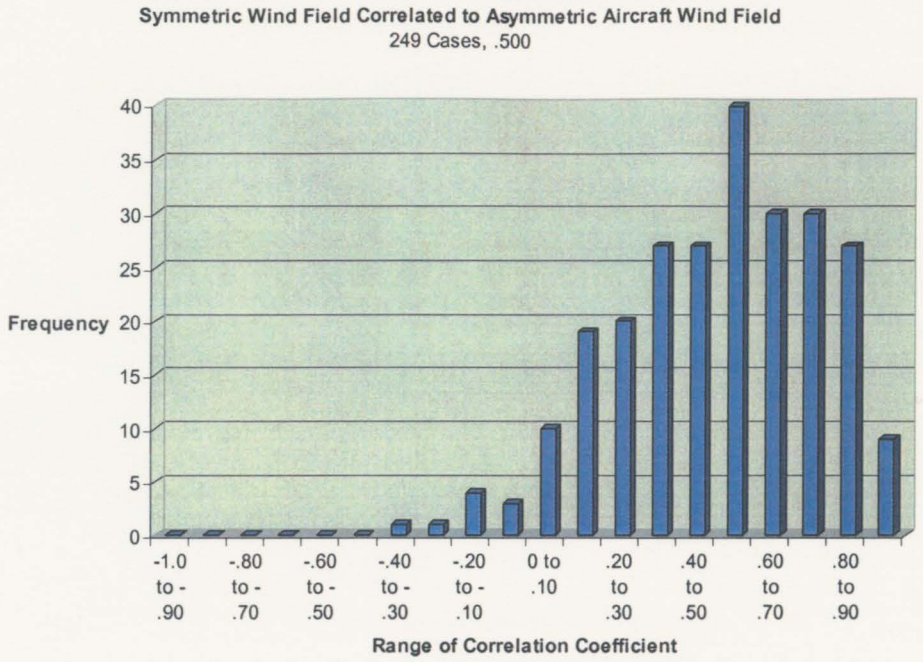

Figure 5.07

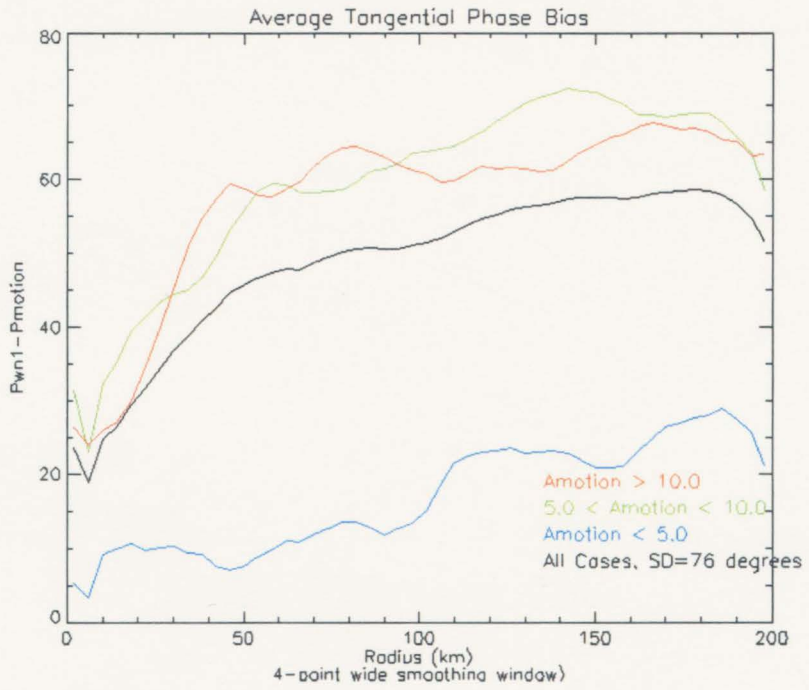

Figure 5.08

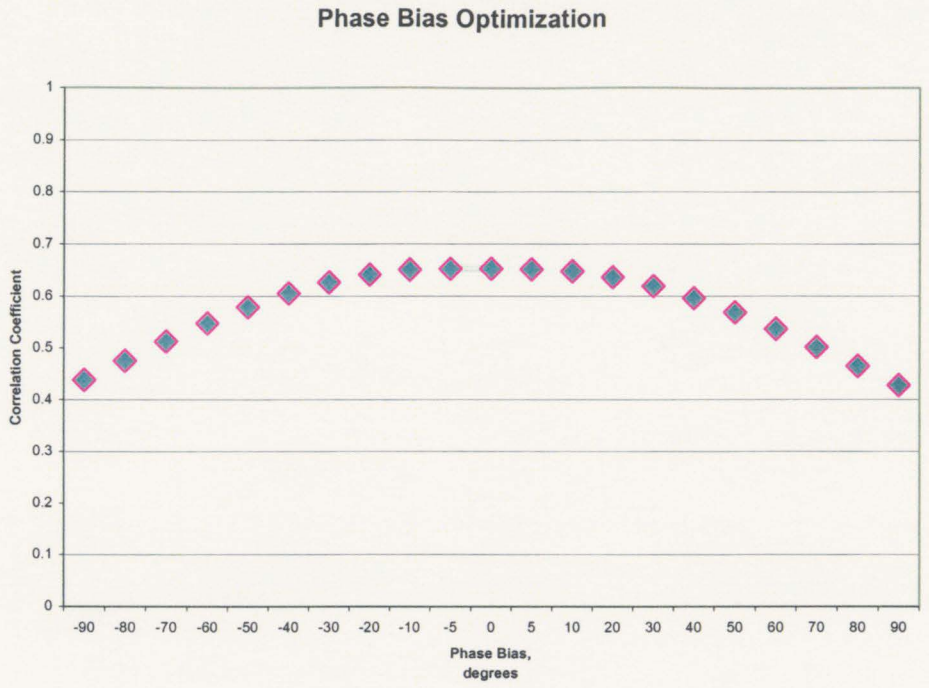

Figure 5.09

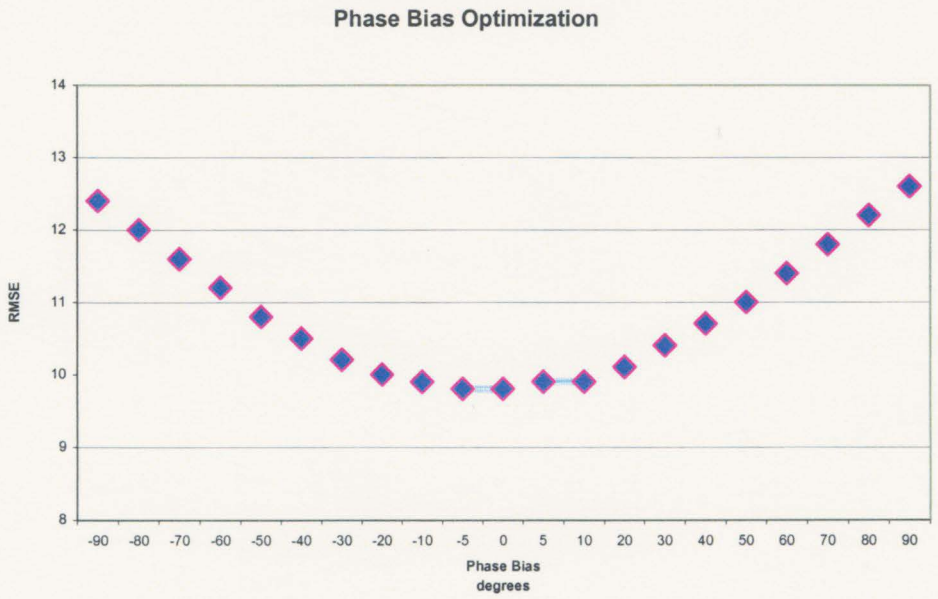

Figure 5.10

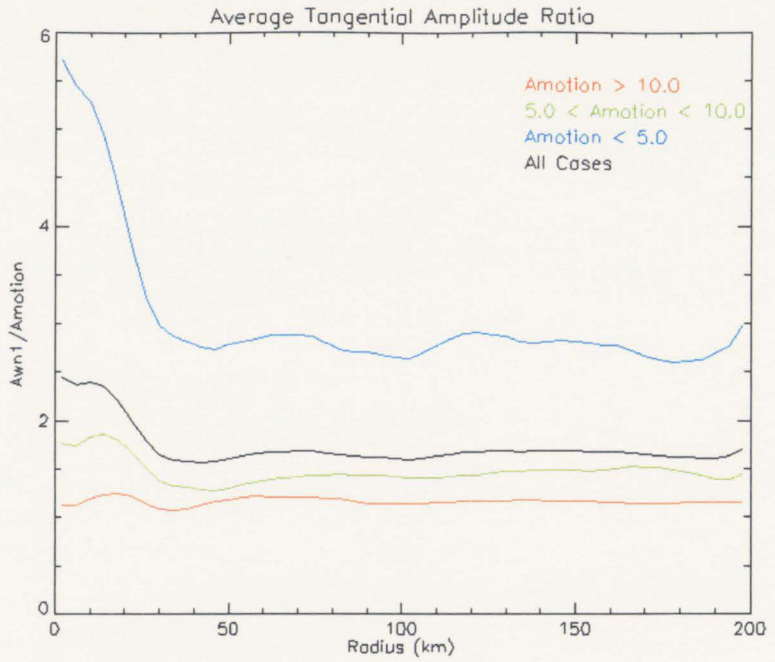

Figure 5.11

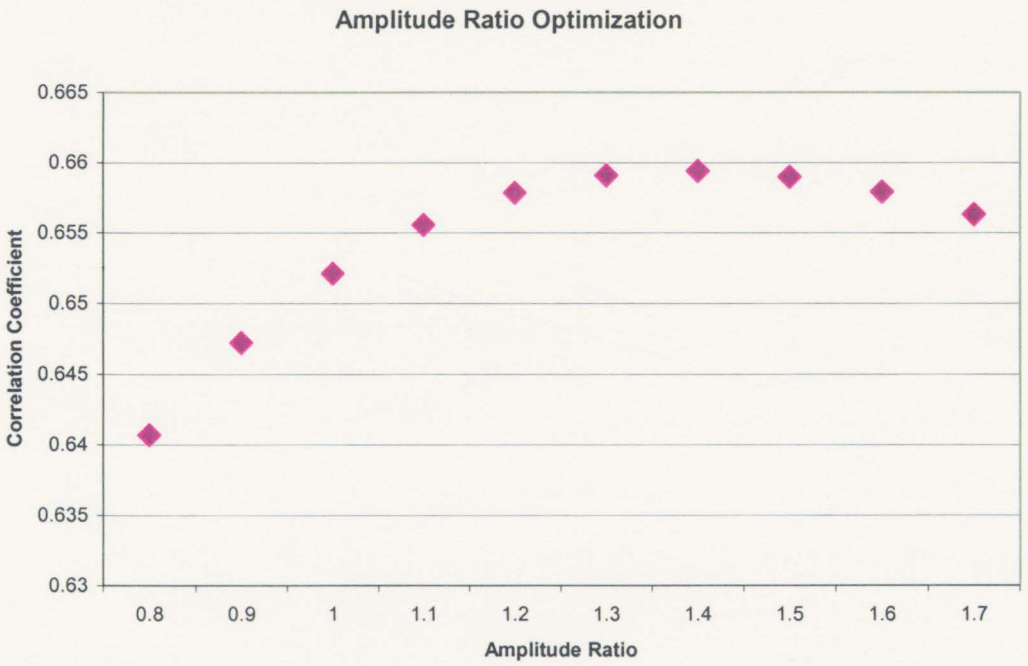

Figure 5.12

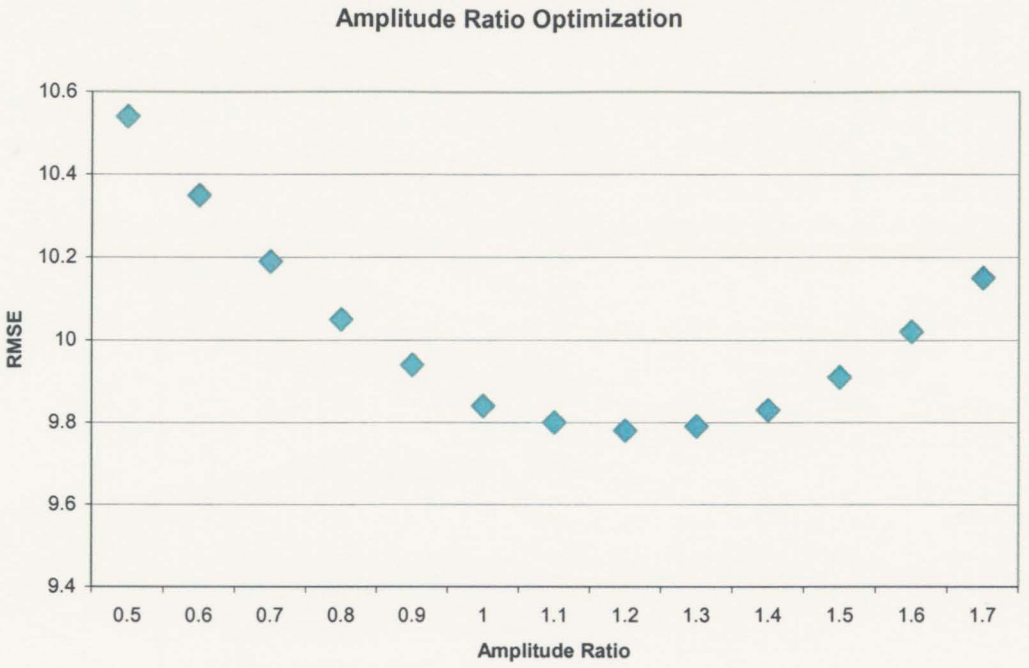
Amplitude Ratio Optimization
RMSE
10.6
10.4
10.2
10
9.8
9.6
9.4
0.5
0.6
0.7
0.8
0.9
1
1.1
1.2
1.3
1.4
1.5
1.6
1.7
Amplitude Ratio

Figure 5.13

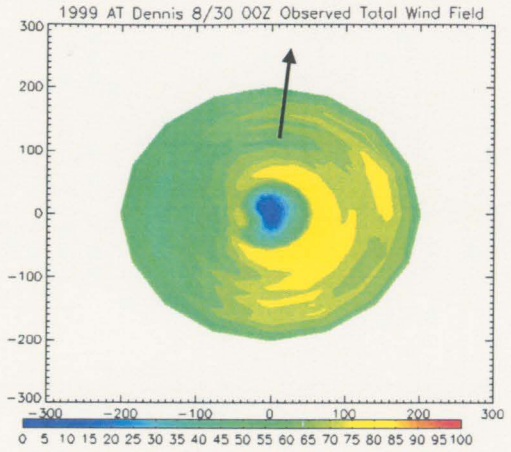

a.

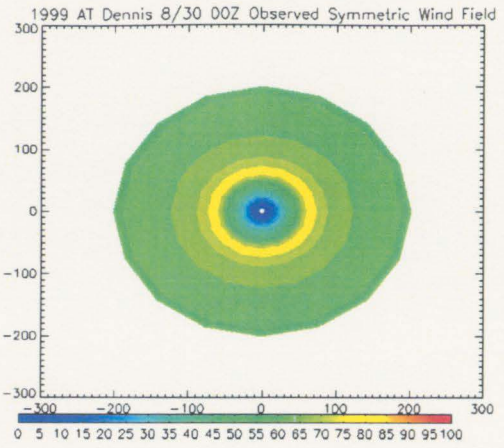

b.

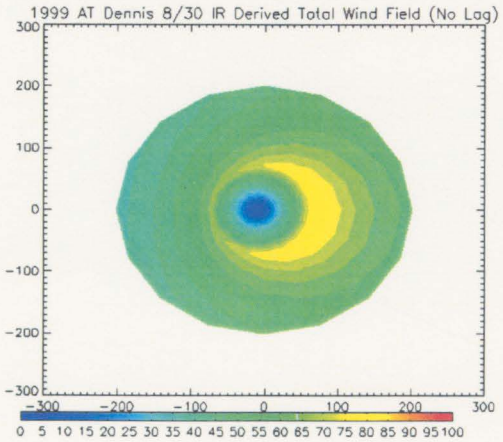

c. Correlation: .910

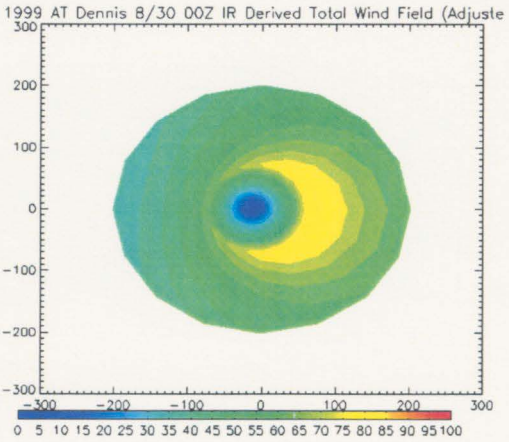

d. Correlation: .883

Figure 5.14

77 knots, 82.7 degree, 10.1 knot heading

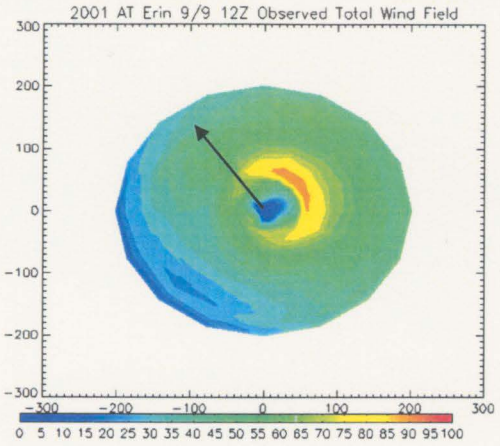

a.

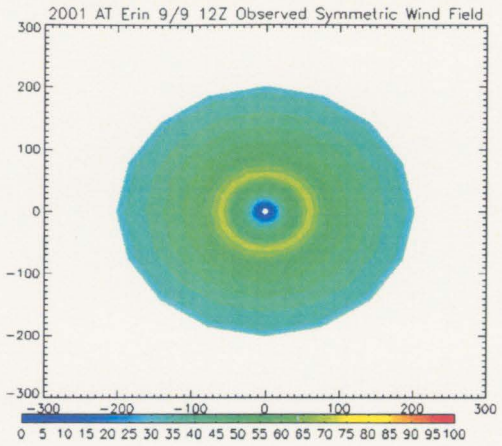

b. Correlation: .661

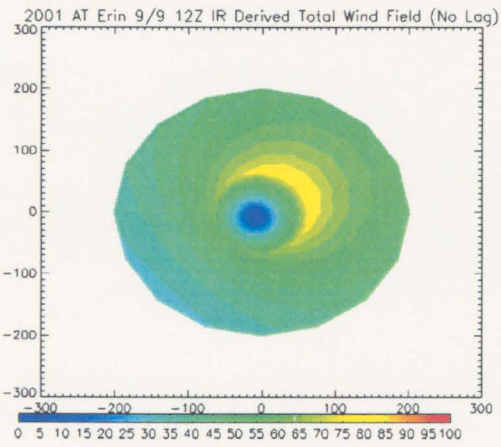

c. Correlation: .796

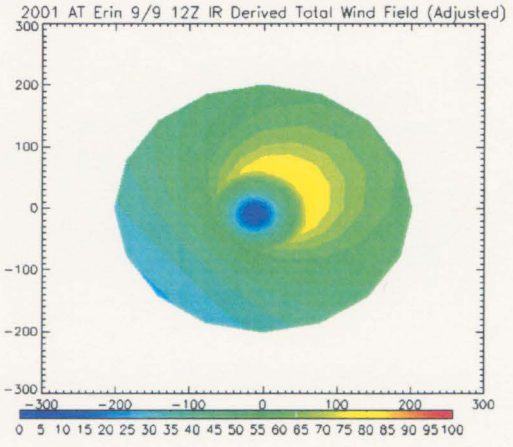

d. Correlation: .752

Figure 5.15

71 knots maxwind, 130.7 degree, 11.9 knot heading.

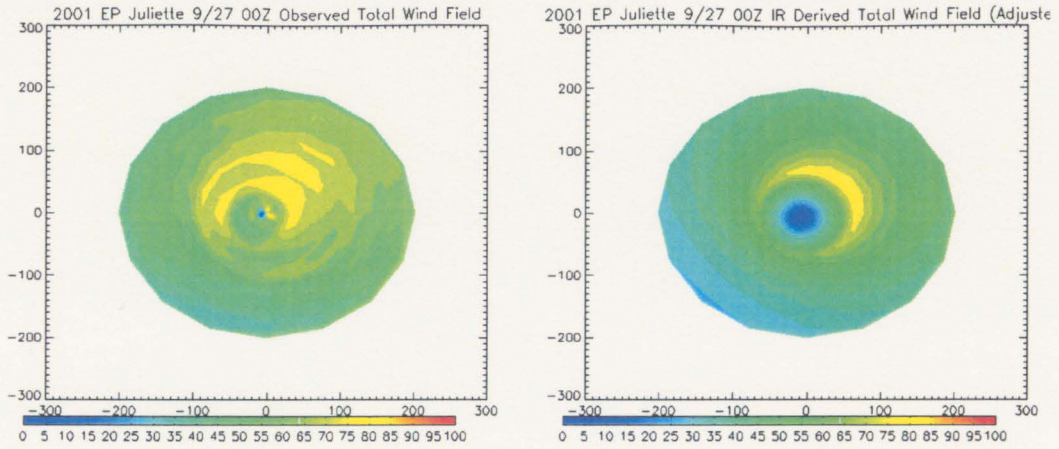

Figure 5.16
Correlation: .547

Table 5.1

CASE	CC	MSR	RMSE
Symmetric Wind Field All Cases (249)	.500	11.7 kts	15.5 kts
Symmetric + Storm Motion Wind Field All Cases (249)	.652	9.8 kts	13.4 kts
Symmetric + Storm Motion Wind Field Amplitude Adjusted All Cases (249)	.659	9.8 kts	13.4 kts
Symmetric Wind Field > .70 2D Correlation (176)	.606	10.6 kts	14.4 kts
Symmetric + Storm Motion Wind Field > .70 2D Correlation (176)	.741	9.6 kts	12.9 kts
Symmetric + Storm Motion Wind Field Amplitude Adjusted > .70 2D Correlation (176)	.743	9.5 kts	12.8 kts

Chapter 6 – Conclusions and Future Work

6.1 CONCLUSIONS

With coastal and island populations booming, and the increased possibility of increased tropical activity due to shifts in the climate, it is necessary to develop a reliable, continuously available method for estimating the wind structure in a tropical cyclone. Because instruments that measure infrared radiation are currently aboard geostationary satellites that provide constant global coverage in the tropics, it is important to utilize this data to predict hurricane wind structure. There are currently no other products that provide continuous monitoring of tropical cyclone activity.

Using aircraft data from 1995-2003 as ground truth, and CIRA infrared archive brightness temperature data, algorithms for objectively predicting the radius of maximum wind and the azimuthally averaged wind speed at a radius of 200 km are developed. Subsequently, a modified Rankine vortex model is used with the IR-derived estimates of radius of maximum wind and wind speed at 200 km to estimate the two-dimensional symmetric wind field in 249 12-hour time periods. Furthermore, the addition of a phase lagged storm motion vector wind asymmetry is added to the 2D symmetric wind field to produce estimates of the total wind field.

The results of this study suggest the IR derived technique for predicting TC wind structure is a dramatic improvement over any other IR derived wind structure estimates. It also appears to be at least as accurate, and more often superior to many any other satellite derived wind structure estimates, if for the simple reason of data availability. Because infrared data from geostationary satellites is nearly continuous with a temporal

resolution of 30 minutes, or better in some cases, there is the capability of producing real-time estimates of hurricane wind structure at least every 30 minutes.

The algorithms work best for tropical cyclone strength cases (>64 knots) that are well organized and moving relatively quickly. Weak tropical depressions and storms are highly un-organized and have complicated structures that are not well represented by a modified Rankine vortex model. Because the entire asymmetric wind field is calculated using a storm motion vector only, slow moving storms are not represented well in the total wind field calculations. The asymmetric wind field in slow moving storms is likely due to factors besides storm motion.

These analyses, theoretically available every 30 minutes, will provide useful information for a variety of people and businesses. First and foremost, the ability to accurately diagnose the location of the maximum wind in a TC, versus simply the magnitude of the maximum wind, is important for ships and islands in the open ocean. A ship will not be safe traveling into an area of greater than gale force winds, therefore, with the aid of the IR derived algorithm for predicting wind structure, the ship will be able to avoid the highest winds. Furthermore, the data is useful to people inhabiting islands in the ocean, for insurance purposes, and of course the purpose of personal safety.

Also of great importance and usefulness is the ability to use this data to intialize weather and wave forecasts. Wave modelers will find information of the location of high winds important for the modeling of storm surges. Weather forecasters will use the additional information about the extent and location of winds to initialize forecast models, to better predict the track and intensity of tropical cyclones.

6.2 FUTURE WORK

Future work in this field is possible and should be undertaken. First and foremost, because the IR algorithm is derived using aircraft data from 1995-2003 as ground truth, it will be necessary to validate the algorithms for the 2004 hurricane season in which the IR data is independent. It can be anticipated that the error might increase slightly, however because the original study consists of a large sample, 249 cases, it is likely that the results will not be significantly worse using independent data.

Clearly, the storm motion vector is not capturing the entire asymmetric flow field for each case, especially for those cases that are slow moving. Therefore, it would be interesting to research the relationship between wind asymmetry and other parameters, including convective asymmetries, relative flow field, and wind shear over the domain. By adding other factors into the asymmetric wind analysis, a closer approximation of the actual wind field should be possible.

It would also be informative and interesting to extend the analysis to include systems in other ocean basins than the Atlantic and East Pacific. The Air Force and NOAA only fly into storms that are a threat to the United States, therefore in order to get ground truth measurements of the wind off of which to base the algorithms, the study had to be confined geographically to the Atlantic and E. Pacific. Clearly, an extension of the analysis to ocean basins in which TC's are NEVER flown is an important step.

Finally, it would be instructive to look into cases in which a concentric eyewall is present, and be able to model these cases using a separate vortex model. Intense tropical cyclones will often have two eyewalls nearly concentric about the center of the storm, the outer eyewall surrounding the inner one (http://amsglossary.allenpress.com/glossary). A

local wind maximum is generally present in each eyewall. Sometimes more than two eyewalls occur. It will be a challenge to incorporate such a vortex model, and to identify cases in which there is a concentric eyewall structure.

Finally, the Aircraft Reconaissance dataset that was developed as part of this project will provide useful and valid information for numerous studies of tropical cyclones. The dataset includes measurements of temperature, dewpoint, altitude, pressure, winds, and location that are highly quality control checked.

References

Ahrens, Donald C., 2002: Meteorology Today: An Introduction to Weather, Climate and the Environment. Thomson Brookscole.

Brueske, Kurt F., Velden, Christopher S. 2003: Satellite-Based Tropical Cyclone Intensity Estimation Using the NOAA-KLM Series Advanced Microwave Sounding Unit (AMSU). *Monthly Weather Review*: Vol. 131, No. 4, pp. 687–697.

DeMaria, M., F.M. Horsfall, and E.N. Rappaport, 1999: Incorporation of aircraft observations into a statistical hurricane intensity prediction scheme. *AMS Conference on Hurricanes and Tropical Meteorology*. 10-15 January, Dallas, TX, Amer. Meteor. Soc.

Demuth, J.L, M. Demaria, J.A. Knaff, and T.H. VonderHaar, 2000: An objective method for estimating tropical cyclone intensity and structure from NOAA-15 AMSU data. *24th Conference on Hurricanes and Tropical Meteorology,* Fort Lauderdale, FL, 484-485

Dunion, Jason P., Velden, Christopher S. 2002: Application of Surface-Adjusted GOES Low-Level Cloud-Drift Winds in the Environment of Atlantic Tropical Cyclones. Part I: Methodology and Validation. *Monthly Weather Review*: Vol. 130, No. 5, pp. 1333–1346.

Dunion, Jason P., Houston, Samuel H., Velden, Christopher S., Powell, Mark D. 2002: Application of Surface-Adjusted GOES Low-Level Cloud-Drift Winds in the Environment of Atlantic Tropical Cyclones. Part II: Integration into Surface Wind Analyses. *Monthly Weather Review*: Vol. 130, No. 5, pp. 1347–1355.

Dvorak, Vernon F. 1975: Tropical Cyclone Intensity Analysis and Forecasting from Satellite Imagery. *Monthly Weather Review*: Vol. 103, No. 5, pp. 420–464.

Holland, Greg J. 1980: An Analytic Model of the Wind and Pressure Profiles in Hurricanes. *Monthly Weather Review*: Vol. 108, No. 8, pp. 1212–1218.

Kidder, S.Q., and T.H. Vonder Haar, 1995: Satellite Meteorology: An Introduction. Academic Press, 466 pp.

Merrill, Robert T. 1988: Environmental Influences on Hurricane Intensification. *Journal of the Atmospheric Sciences*: Vol. 45, No. 11, pp. 1678–1687.

Rao, P. Anil, Velden, Christopher S., Braun, Scott A. 2002: The Vertical Error Characteristics of GOES-Derived Winds: Description and Experiments with Numerical Weather Prediction. *Journal of Applied Meteorology*: Vol. 41, No. 3, pp. 253–271.

Velden, Christopher S., Olander, Timothy L., Zehr, Raymond M. 1998: Development of an Objective Scheme to Estimate Tropical Cyclone Intensity from Digital Geostationary Satellite Infrared Imagery. *Weather and Forecasting*: Vol. 13, No. 1, pp. 172–186.

Velden, Christopher S., Hayden, Christopher M., Paul Menzel, W., Franklin, James L., Lynch, James S. 1992: The Impact of Satellite-derived Winds on Numerical Hurricane Track Forecasting. *Weather and Forecasting*: Vol. 7, No. 1, pp. 107–119.

Willoughby, H.E., M.E. Rahn, 2003: The Climatology of Hurricane Wind Profiles. *25th Conference on Hurricanes and Tropical Meteorology.* 29 April—3 May 2002, San Diego, CA